Macalester Journal of Physics and Astronomy

Volume 10
Issue 1 *Spring 2022*

Article 7

May 2022

Hunting for Fast Radio Bursts from Messier 82: Exploring the FRB--Magnetar Connection

Susie Paine
Macalester College, spaine@macalester.edu

Hunting for Fast Radio Bursts from Messier 82: Exploring the FRB–Magnetar Connection

Abstract

Fast radio bursts (FRBs) are short-duration radio pulses of cosmological origin. Among the most common sources predicted to explain this phenomenon are bright pulses from a class of extremely highly magnetized neutron stars known as magnetars. In 2020, a Galactic magnetar produced an FRB-like burst, allowing researchers to constrain the Galactic magnetar burst rate. We assume that the magnetar burst rate scales with star formation rate and test an important prediction for similar bursts in nearby galaxies. Messier 82 (M82) has a star formation rate 40 times that of the Milky Way, implying that the magnetar burst rate would be quite high. We observed M82 with the 20 meter telescope at the Green Bank Observatory for 28.2 days. We found 291 candidate bursts, but none of those candidates had a signal-to-noise ratio greater than 10. An S/N of 10 is required for a candidate burst to be considered an FRB. Additionally, none of the repeating dispersion measures (DMs) we found had enough bursts to constitute a confidence level of 5 sigma. Using these constraints, we determined an upper bound for M82's magnetar burst rate to be 0.035/day. Based on this result, we determined that star formation rate cannot scale with magnetar burst rate in the case of M82.

MACALESTER COLLEGE

Hunting for Fast Radio Bursts from Messier 82: Exploring the FRB–Magnetar Connection

by

Susie Paine

in the

Department of Physics and Astronomy

Advisors: Duncan Lorimer, John Cannon

April 2022

MACALESTER COLLEGE

Abstract

Department of Physics and Astronomy

by Susie Paine

Fast radio bursts (FRBs) are short-duration radio pulses of cosmological origin. Among the most common sources predicted to explain this phenomenon are bright pulses from a class of extremely highly magnetized neutron stars known as magnetars. In 2020, a Galactic magnetar produced an FRB-like burst, allowing researchers to constrain the Galactic magnetar burst rate. We assume that the magnetar burst rate scales with star formation rate and test an important prediction for similar bursts in nearby galaxies. Messier 82 (M82) has a star formation rate 40 times that of the Milky Way, implying that the magnetar burst rate would be quite high. We observed M82 with the 20 meter telescope at the Green Bank Observatory for 28.2 days. We found 291 candidate bursts, but none of those candidates had a signal-to-noise ratio greater than 10. An S/N of 10 is required for a candidate burst to be considered an FRB. Additionally, none of the repeating dispersion measures (DMs) we found had enough bursts to constitute a confidence level of 5σ. Using these constraints, we determined an upper bound for M82's magnetar burst rate to be 0.035 day^{-1}. Based on this result, we determined that star formation rate cannot scale with magnetar burst rate in the case of M82.

Acknowledgements

To repeat the cliché of everyone who has ever written an Acknowledgments section, there is neither enough time nor space for me to fully express my gratitude to these individuals (and countless others) for their support through this endeavor. I must, however, make at least a drop in the bucket.

Macalester College has been an integral step on my journey. I am certain that I would not have been able to produce a thesis of the same quality at another institution without the widespread and complete support I have received at every step of my journey.

The Physics & Astronomy Department has been the perfect place for me to start my higher educational journey, and I will be forever grateful for the help that the department has given me at every stage. Since the class I observed during my Spring Sampler, I have been certain that this department is an excellent place to be a student and a person, and I was proven correct again and again.

The class I observed on my Spring Sampler was John Cannon's Modern Astronomy course. Later that day, I went to John's office hours and asked about Mac's telescope. He walked me up the stairs to the Mac Observatory, and I knew that I would come to Macalester. There are many things I need to thank John Cannon for. Firstly, my time at this college and in this department. John asked me to do summer research with him... twice. He advised me through four years of academics. After all of this, he wrote many, many letters of recommendation to REUs and to grad schools. His patience and kindness throughout the thesis process has been invaluable. Especially since I often forget about meetings. John, I will be forever grateful for your time, your attention, and your belief in my abilities.

I must also thank Anna Williams for all her help. Anna has taught as many of my classes as John, and she has been just as wonderful. She has always been interested in my research, giving me valuable feedback on my presentations. She has also written countless letters of recommendation for me, as well as agreeing to sit on my honors committee. Her comments on this thesis greatly improved its quality. Anna, thank you for all the hours you have spent teaching me.

In addition to Macalester, I have also been supported by the Physics & Astronomy Department at West Virginia University. The summer of 2021 was a whirlwind, but I loved it. Seeing the Green Bank Telescope in motion gave me the inspiration I needed to continue this project, and the department gave me the support I needed to finish it.

Maura McLaughlin agreed to sit on my honors committee after a long, chaotic email. She then read my thesis with a fine-toothed comb, helping me understand the necessary astronomy and clarify my writing. Every time I've talked to Maura, I've felt better after the experience. Maura, thank you for all your help with this project, and I look forward to collaborations to come.

The most pertinent thanks for this thesis go to Duncan Lorimer, my advisor for the past ten months. I have been interested in fast radio bursts since I first read about them in my junior year of high school. I obviously jumped at the chance to work with the author of their discovery paper. I am so grateful that I was selected to work with Duncan and even more grateful for his support throughout this project. This work has been the highlight of my academic life (thus far), and I am so grateful for this opportunity. Duncan, I will be forever grateful for your support, your explanations, and your continuous revisions of this thesis.

Now that I've gotten the professors out of the way, it's time for me to thank some of my peers.

Jordan Stanley worked on this project with me in the summer of 2021. Because she had prior experience with the work, her experience was a necessary bridge for me. Also, I may not have survived that summer without someone to commiserate about coding with.

One of the most important acknowledgments in this thesis must go to Alyssa Bulatek. We met on the second floor of the CC after John put us in contact. You told me I should go ahead and take Modern Physics first semester. You were certain I would make it through. And I did. The next semester, you patiently walked me through the vast majority of the Astrophysics homework problems. I thought—still think—that you were/are the coolest person ever. I wanted to follow in your footsteps—and I did. Alyssa, thank you for clearing the path. And

thank you for knowing how to code in Python, since I'm still not sure how to make basic plots.

Although she didn't have a direct impact on this thesis, I must also thank Lilly Bralts-Kelly for being one of the most kick-ass people I've ever met. Watching Lilly finish her capstone taught me a lot about how to live with my work without letting it consume me. Plus, she inspired me to get my first tarot deck. Lilly, the High Priestess, thank you for the inspiration.

I must also thank Plearth for all of their love and support through the years. Most of the magic of college is the people you share it with along the way.

Although she is a chemist, Maddy Rodemeier has been an integral part of my support system for the past four years. We've come a long way from our days doing calculus homework on Dupre 5, but there's no one I would have rather done it with. I've spent more time with Maddy than any other human being over the past two years. If you listen to us talk, you can tell. This thesis owes its existence in part to Maddy reminding me to suck it up and write every day. Maddy, thank you for your daily efforts to keep me sane (or not), and for loving Buffy the Vampire Slayer as much as I do.

Penultimately, I have to thank Ira Langdon. It would take me a thesis worth of pages to fully express my gratitude to Ira. I could not ask for a better best friend. Ira, thank you for comforting me when I cried, smiling when I laughed, and laughing when I inevitably did something worth laughing at. Thank you for the hours of science fiction TV viewing, the days of pointless philosophical arguments, and the countless heart-to-heart talks. Thank you for telling me which figures look good, remaking my slides for me, and holding my hand when I panicked and panicked and panicked about this thesis. Thank you for never judging me (until I did something like walk into a door). Most importantly, thank you for being my friend. I may live the rest of my life trying to deserve it.

Last in this list but first in my heart, I am eternally grateful to my family. Each and every one of them has been so supportive of me, in their own unique way. I am beyond blessed to be related to these people.

Beth: Thank you for loving me so much that you never want me to leave. The worst part of growing up is leaving you. Thank you for letting me feel smart by teaching you math and forcing me to watch television from the 1960s and the 2000s. You're gonna go far, kid.

Joe: Thank you for not calling me short every time you see me. I'm glad you love math so much—one day I'm going to ask *you* for help with *my* homework. Thank you for letting me help you with physics. If you follow your passion (math), it will lead you home.

Amy: I thought I would hate that you came to Macalester, but it has been one of my greatest joys to watch you grow here. You've changed from an insecure, uncertain girl to a confident woman. I'm so glad to have spent so much time with you, and I wouldn't change it for anything. Loud and high-energy, honey, you've got this!

Dad: I miss riding in the car listening to you talk about baseball scores. I still don't know anything about baseball, but I know a lot about history (and you may know something about astronomy). Thank you for keeping track of new space race books on the B&N newsletter. Thank you for driving through Wisconsin over a dozen times to get me to and from college. Thank you for telling terrible jokes that you think are hilarious. Thank you for talking even when you know I'm not listening. Thank you for everything. I love you, Dad.

Mom: I wish I was curled up with you on the couch. Every time you hug me, I feel like a little kid again. Thank you for that. Thank you for making my appointments for me, even though I'm an adult. Thank you for answering three phone calls a day if I need you. Thank you for coaching me through answering official emails. Thank you for asking me about my life every time we talk. Thank you for remembering which of my friends studies what. Thank you for pushing me towards my dreams when I'm too nervous to go for them. Every time, I needed the push. Thank you for everything. I love you, Mom.

To the whole family: I would not have gotten here without you. I love you lots and lots.

This project was funded by the National Science Foundation through the Research Experiences for Undergraduates program at West Virginia University. The telescope time was paid for by the Research Corporation for Science Advancement.

Contents

List of Figures

List of Tables

CHAPTER 1: Introduction

Astronomical phenomena can be split into two categories: transient and non-transient objects. Non-transient objects like galaxies and stars persist far beyond a human lifetime. Astronomers study changes in these objects by observing large populations and modelling how one object might go through different life stages. Transient objects, like gamma ray bursts and supernovae, change on timescales that are readily observable by humans. Many of these events take place over fractions of a second. Transient events are difficult to detect because a telescope has to be looking at just the right point in the sky at just the right time.

The history of radio transients is filled with fortuitous discoveries. The major category of transient objects in radio astronomy is pulsars. Their characteristic repeating pulses were discovered by Jocelyn Bell Burnell in 1967 (Hewish et al. 1968). Pulsars have become a large field in the past decades, with thousands known and surveys to discover them at every major radio telescope. In a pulsar survey targeting the Magellanic Clouds in 2001, an unusual radio pulse was recorded by the Parkes Radio Telescope. In 2007, an undergraduate student at West Virginia University was reviewing archival data and discovered this burst (Lorimer et al. 2007). Now, it is known as the Lorimer Burst, the first fast radio burst (FRB), pictured in Figure 1.1.

Since the Lorimer Burst, FRBs have been detected by 14 radio telescopes, including the Arecibo Observatory, Robert C. Byrd Green Bank Telescope (GBT), Karl G. Jansky Very Large Array (VLA), and the Canadian Hydrogen Intensity Mapping Experiment (CHIME). Over 790 separate bursts have been detected (Spanakis-Misirlis 2021). Though detection rates were slow in the first few years after discovery, FRBs have been detected in much greater numbers in recent years. Much of this uptick in discovery is due to CHIME's large instantaneous sky coverage and total time on sky, leading to a high discovery rate.

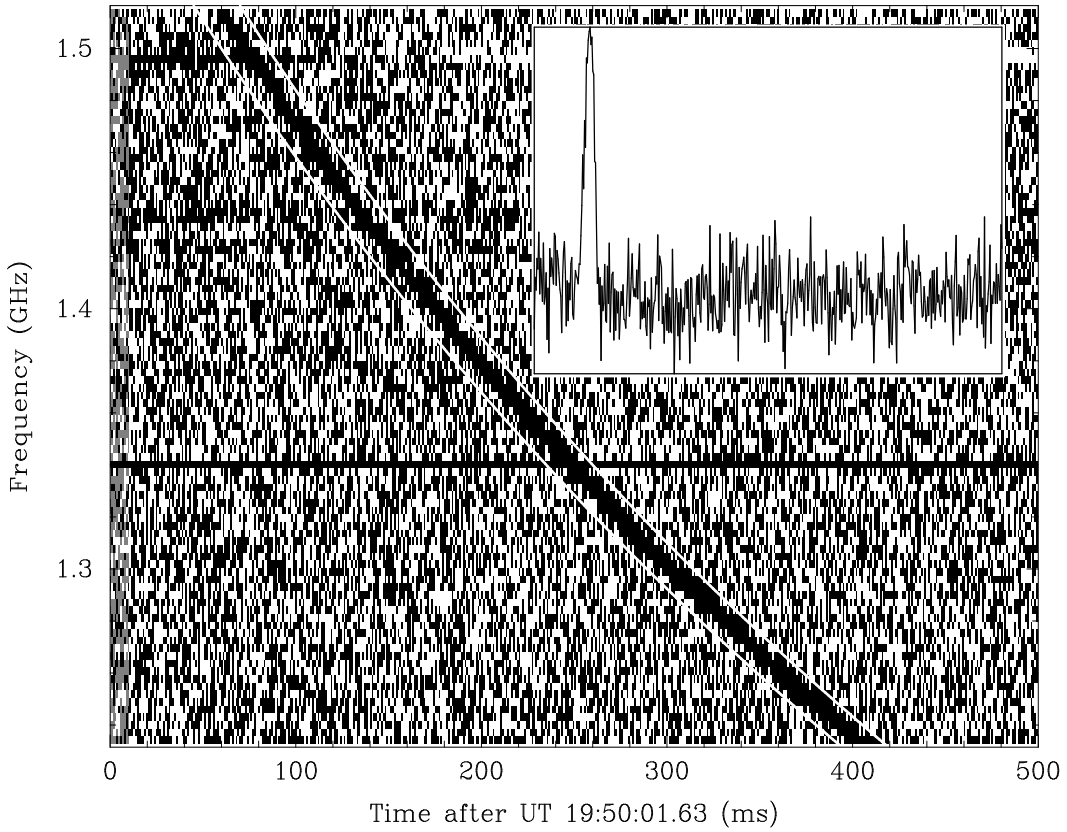

FIGURE 1.1: The Lorimer Burst was found in 2007 by an undergraduate at West Virginia University. The dispersed burst is pictured in the waterfall plot above, showing radio frequency versus time. The dedispersed pulse shape is shown in the inset graph in the upper right corner. (Lorimer et al. 2007)

1.1 Overview of Fast Radio Bursts

Fast radio bursts are best summed up by their name. They are millisecond pulses of radio emission. Some are as brief as 0.24 ms, while others are much longer, up to 5,000 ms (Spanakis-Misirlis 2021). Searches for FRBs occur over a wide range of frequencies. Most FRB searches have large bandwidths, which typically contain 1420 MHz. Fast radio bursts only have a few observable properties: sky position, flux density, pulse width, and dispersion measure (Petroff et al. 2019). Sky position simply means the position of the burst on the sky. For most bursts, this is not a precise location, but a possible area. Single dish telescopes, like the GBT, cannot determine a location more precise than their beam size, leading to position uncertainties in most FRB detections. Interferometers, like the VLA and

CHIME, provide more precise location data, but beam sizes still pose a problem for precise localizations. Precise positional data is necessary to determine an FRB's native galaxy. I discuss FRBs with host galaxy localizations in Section 1.1.1 below.

The next observable property of fast radio bursts is the flux density. This quantity is a measure of brightness and the burst's total energy, modulated by distance. However, FRBs are detected at particular frequencies, so most FRB fluxes are quoted as flux densities, referring to the flux at a particular frequency. Most flux densities are listed as the highest value for any frequency observed for a particular burst. The pulse width, the third observable property of FRBs, is the temporal length of the burst. Most bursts only last for milliseconds, but those lengths are still measurable, in many cases. Figure 1.2 shows the flux densities versus pulse widths for known FRBs. Generally, FRBs have a pulse width of 1-10 ms and a flux density of about 1-10 Jy.

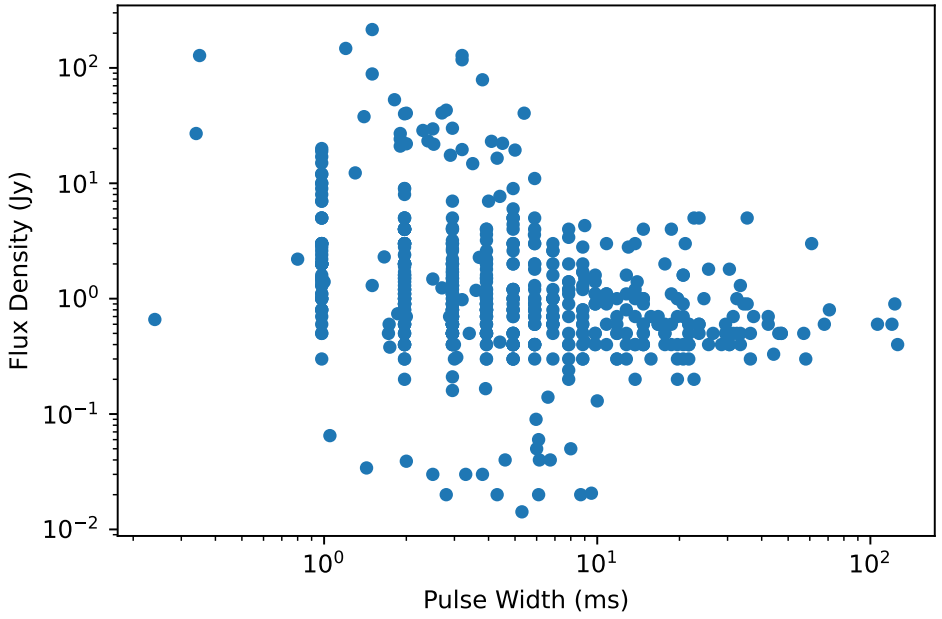

FIGURE 1.2: The relationship between the flux densities and pulse widths of known FRBs are shown above. The flux densities, on the y-axis, span about five orders of magnitude. The pulse widths, on the x-axis, span about four orders of magnitude. The banded structures in the figure are due to rounding effects in different FRB catalogs. The data in this figure was accessed from Spanakis-Misirlis (2021).

Fast radio bursts are dispersed into a characteristic exponential decay. This dispersion is due to the differential interactions with intervening material. As a photon travels between an FRB progenitor and the Earth, it passes through gases, both neutral and ionized. Free electrons in the burst's path disperse the photons, and therefore delays their arrival times. Photons with lower frequencies are dispersed more than those with higher frequencies, meaning that higher frequencies reach the telescope before lower frequencies. This dispersion generally leads to a somewhat quadratic curve in frequency vs time space, as seen in Figure 1.1. The total time delay between the highest and lowest frequencies,

$$\Delta t = 4150 \text{ s} \, (\nu_{\text{lo}}^{-2} - \nu_{\text{hi}}^{-2}) \, \text{DM}, \tag{1.1}$$

where ν_{lo} and ν_{hi} represent the high and low frequencies of a particular observation in units of MHz (Lorimer & Kramer 2004). Dispersion measure (DM) in this formula corresponds to the level of dispersion in units of cm^{-3} pc. The DM is dependent on the amount of material the burst has passed through, and is defined physically as,

$$\text{DM} = \int_0^d n_e(l) \, dl, \tag{1.2}$$

where d is the distance to the FRB progenitor, n_e is the electron number density, and l is a path length through the electron density (Petroff et al. 2019). When the electron density is relatively constant across space, Equation 1.2 reduces to a simple product of electron density and distance.

In general, more distant bursts will have a higher DM than closer bursts. However, DM is also dependent on the material around the burst and the material of the Milky Way. If an FRB progenitor is located in an area of particularly dense gas, the DM will be larger than a progenitor in a less dense area, even if the two objects are the same distance from Earth. Thus, DM can only be used as a rough estimate of distance rather than a specific measure. If the DM contribution of the host galaxy and the Milky Way can be determined, DM can be used as a much more sophisticated distance estimate. Based only on these rough estimates, astronomers theorized that FRBs come from extragalactic sources. More recently, FRBs were localized to specific galaxies, confirming their extragalactic status. Generally, the DM of the Milky Way is on the order of 30-50 cm^{-3} pc in the halo and an order of

magnitude higher in the disk. The DMs of known FRBs are shown in a histogram in Figure 1.3. The histogram peaks at about 300 cm^{-3} pc, comfortably outside of Galactic range in the halo. Generally, FRBs are located outside of the Galactic plane so the DM contribution from the Milky Way is on the low end.

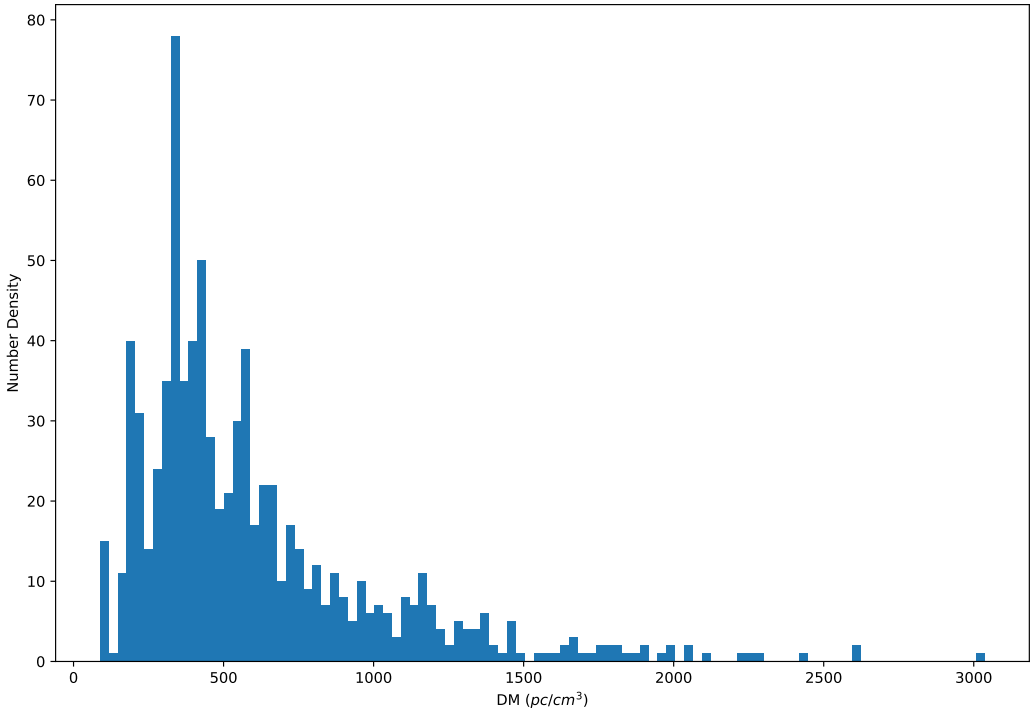

FIGURE 1.3: This figure shows the distribution of dispersion measures in the known FRB population. Most FRB DMs are centered at about 300 cm^{-3} pc. FRBs are extragalactic, so they do not populate the lowest end of the DM spectrum. Galactic pulsars would fill the lowest end of DM space. There is a tail at higher DMs because more distant objects are harder to detect.

In Figure 1.4, the DMs of known FRBs are plotted against their flux densities. If all FRBs had the same luminosity, we would expect a trend that lower DMs correspond to higher flux densities. From the figure, this is not the case, due both to differing luminosities and the fact that DM is not equal to distance.

Initially, astronomers thought that FRBs were created in cataclysmic processes, or processes that result in the destruction of their hosts. However, in 2016, on routine follow-up observations of FRB 121102, repeating pulses were found (Spitler et al. 2016). Astronomers had been periodically observing in the direction of all FRBs, hoping to find further evidence of the events that led to the burst. On

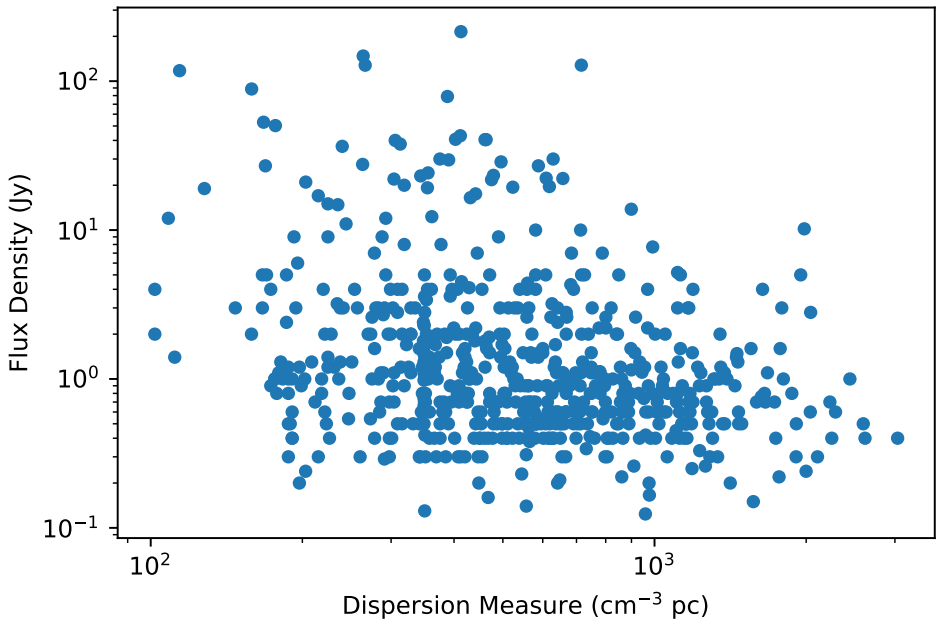

FIGURE 1.4: The relationship between flux density and dispersion measure for the known FRB population. The banded structures within the plot are due to rounding effects in different FRB catalogs. This plot does not show the faintest FRBs to better illustrate the relationship between flux density and DM. Generally, FRBs with lower DMs have higher flux densities.

this particular observation, Spitler et al. (2016) discovered 10 bursts within a short time frame, conclusively proving that FRB 121102, at least, had not been caused by a destructive event. By early 2022, over 20 bursts have been found from FRB 121102 (Spanakis-Misirlis 2021). Since the surprise discovery of FRB 121102, 23 other repeating FRBs have been found. Repeating FRBs have produced over 100 bursts in total.

However, the vast majority of FRBs are non-repeating. There are two possible explanations for the low numbers of repeating FRBs. Either all FRBs repeat, but repeated bursts are harder to detect for some sources, or there are two distinct FRB populations. It is possible that many FRBs are repeating, though more bursts have not been detected. There is a lot of variation between different bursts of repeating FRBs. There are differences of two orders of magnitude in flux from different bursts from FRB 121102 (Petroff et al. 2019). However, the DM and location are consistent, confirming that the bursts arise from the same source. It

is certainly possible that many, or most, non-repeating FRBs simply do not have repeated bursts detected.

Recent work suggests, however, that repeating FRBs and non-repeating FRBs are morphologically distinct. After the release of the first CHIME FRB catalog in the summer of 2021 (Masui & Chime/Frb Collaboration 2021), researchers could begin to run statistical analyses of large numbers of FRBs. These analyses indicate that there are two populations of FRBs (Lorimer 2021). It might even be possible to determine whether an FRB will repeat from a single burst (Lorimer 2021).

Repeating FRBs typically have longer pulses than non-repeating bursts (Zhong et al. 2022). Repeating bursts also have smaller emission bandwidths, generally about 100-200 MHz, while non-repeating bursts often fill the entire CHIME bandwidth (400-800 MHz) (Zhong et al. 2022). In addition to smaller bandwidths, repeaters have higher peak frequencies than their non-repeating counterparts. Zhong et al. (2022) examine if the differences between those populations cannot be due to beaming effects. Beaming effects, in short, are changes in a pulse's appearance based on the geometry of the beam relative to Earth. If a beam is pointed directly at Earth, a telescope sees a different beam shape than a beam that is pointed glancingly at Earth. The differences between the two populations are not just limited to the geometry of the burst; burst length and peak frequency are also different between the populations. Beaming effects cannot explain all these differences, leading Zhong et al. (2022) to conclude that repeating and non-repeating FRBs must be produced in different ways.

1.1.1 Localizations of Fast Radio Bursts

FRBs have been discovered across the sky, as shown in Figure 1.5. All known FRBs have been plotted in Galactic coordinates. There seems to be a position dependence in the distribution. This positional dependence is likely a survey effect. Theoretically, FRBs should be equally distributed across the sky. However, radio telescopes are not evenly distributed over the surface of the Earth. CHIME, the current best FRB detector, is located in the Northern hemisphere, leading to an overdensity of detections above the Galactic Equator and an underdensity below

it. Additionally, CHIME is most sensitive to bursts in the center of its beam. Due to CHIME's position, this means that it is most sensitive to FRBs with a declination around +50 degrees. With a CHIME-like telescope in the Southern hemisphere, FRBs' apparent positional dependence should disappear.

CHIME is a particularly good FRB detector because of its large beam size. A larger beam means that the telescope can see more of the sky at once, raising the likelihood of a detection. The downside of such a large beam is a greater positional uncertainty. A telescope with a smaller beam, such as an interferometer like ALMA, while it has greater positional accuracy, is less likely to make a detection.

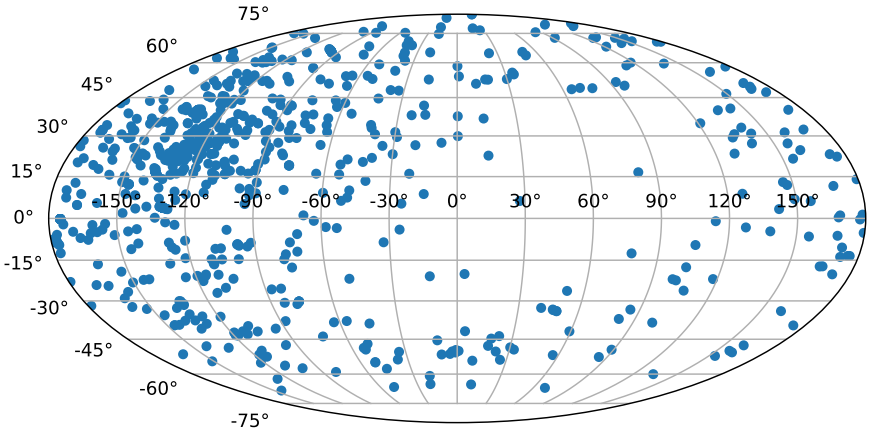

FIGURE 1.5: This figure shows a map of all known FRBs on the sky plotted in Galactic coordinates, as of April 2022. At that date, 796 FRBs had been found. The overdensity on the left side of the plot represents a line of about +50 degrees in declination, the location where CHIME is most sensitive to FRBs. The underdensity on the right is due to the relative lack of FRB detecting telescopes in the Southern hemisphere.

Given the high dispersion measures of known fast radio bursts, astronomers were eager to determine precise localizations for FRBs. Those localizations would point to whether FRBs were galactic or extragalactic, based on what objects are in the

line of sight. FRB 121102 was the first FRB to have a precise localization. Much of this fact is simply due to the larger amount of data on FRB 121102. With high time-resolution data, FRB 121102 was localized to a precision of about 100 milliarcseconds (Chatterjee et al. 2017). This localization was precise enough to determine that FRB 121102 is coincident with a dwarf galaxy with a redshift of $z = 0.193$, which corresponds to a distance of about 1 Gpc. FRB 121102 was determined as definitively extragalactic, with a low-metallicity, low-mass dwarf host galaxy (Tendulkar et al. 2017). Since FRB 121102, about 19 FRBs have been localized, including some non-repeating bursts (Petroff et al. 2021). These FRBs have a wide variety of host galaxies, slightly confounding theorists trying to determine the FRB progenitor. Most of these localizations were achieved by the Australian Square Kilometer Array Pathfinder (ASKAP), a powerful interferometer.

1.2 Motivation for this Thesis

In 2020, an FRB-like burst was detected from a Galactic magnetar (Bochenek et al. 2020; CHIME/FRB Collaboration et al. 2020). The magnetar in question, SGR 1935+2154, was in a period of unusually high X-ray activity at the time. The radio burst had a similar profile to known FRBs. There is some debate about whether this Galactic burst can be classified as an FRB, since it is much dimmer than any known extragalactic FRB, as shown in Figure 1.8. However, this FRB-like burst creates an important link between magnetars and FRBs.

We expect that the magnetar burst rate from a particular galaxy will scale roughly with star formation rate. Our target is Messier 82, or M82, a nearby starburst galaxy, which should have a higher number of magnetars than other galaxy types. Further discussion of M82 is given in Section 1.2.3. If FRBs do arise from magnetars, there should be a higher FRB rate from M82 than other galaxies. Starburst galaxies generally have a star formation rate about 40 times higher than the Milky Way, meaning that the rate of magnetar formation is also roughly 40 times higher. Additionally, a burst from M82 with a similar flux as SGR 1935+2154 would be

clearly observable with a relatively modest telescope. Using results from Bochenek et al. (2020), Hawkins & Lorimer (2021) predicted the likely number of bursts found from M82 over time.

Bochenek et al. (2020) gives an all-sky FRB rate of about 3.6 bursts/sky/year for bursts within the Milky Way. Figure 1.6 shows the probability density using Poissonian analysis around Bochenek et al. (2020)'s value. The probability density of the rate is defined as,

$$P(R) = RTe^{-RT}, \tag{1.3}$$

where T is the total time observed by Bochenek et al. (2020), 0.468 years. The most likely burst rate in this probability density is ∼2.5 bursts/sky/year in the Milky Way, or slightly lower than the value quoted in Bochenek et al. (2020).

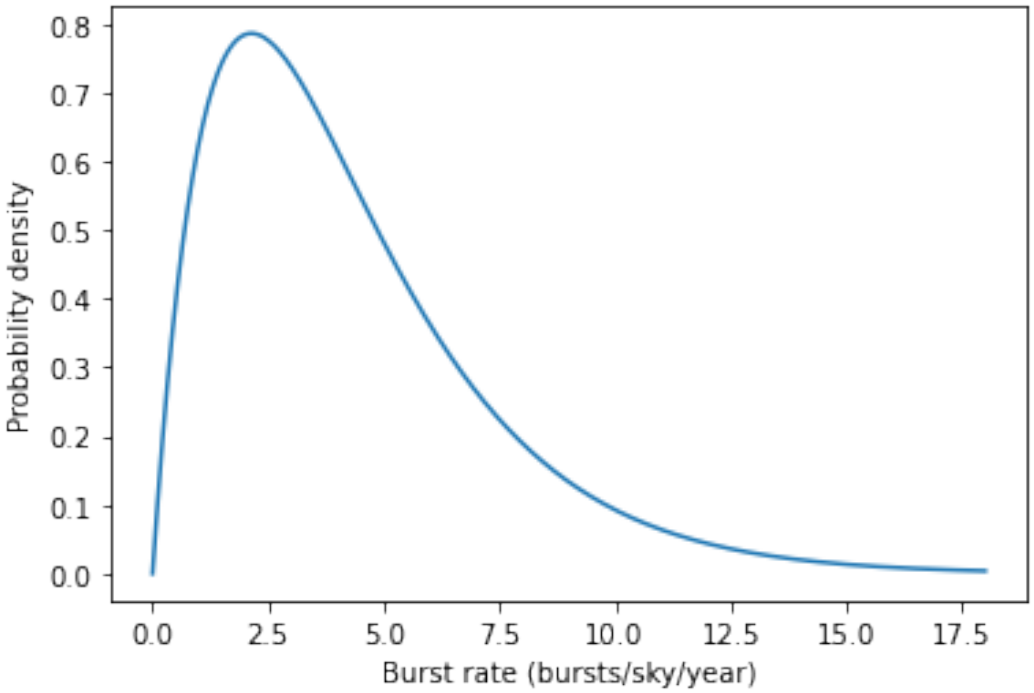

FIGURE 1.6: An estimate of the burst rate from Galactic magnetars similar to SGR 1935+2154. A burst rate of about 2.5 bursts/year from Galactic magnetars is most likely (Hawkins & Lorimer 2021).

Taking the 95% confidence interval from the probability density in Figure 1.6, we then multiply by a factor of 40 to find the magnetar burst rate in M82, in accordance with our hypothesis that magnetar burst rate scales with star formation rate. We then take those bounds and plot the number of FRBs we expect to find

after a length of time in Figure 1.7. The red shaded region represents the possible range of FRBs found by that time. We anticipate an FRB detection using the 20 m telescope within the first ∼25 days of observation.

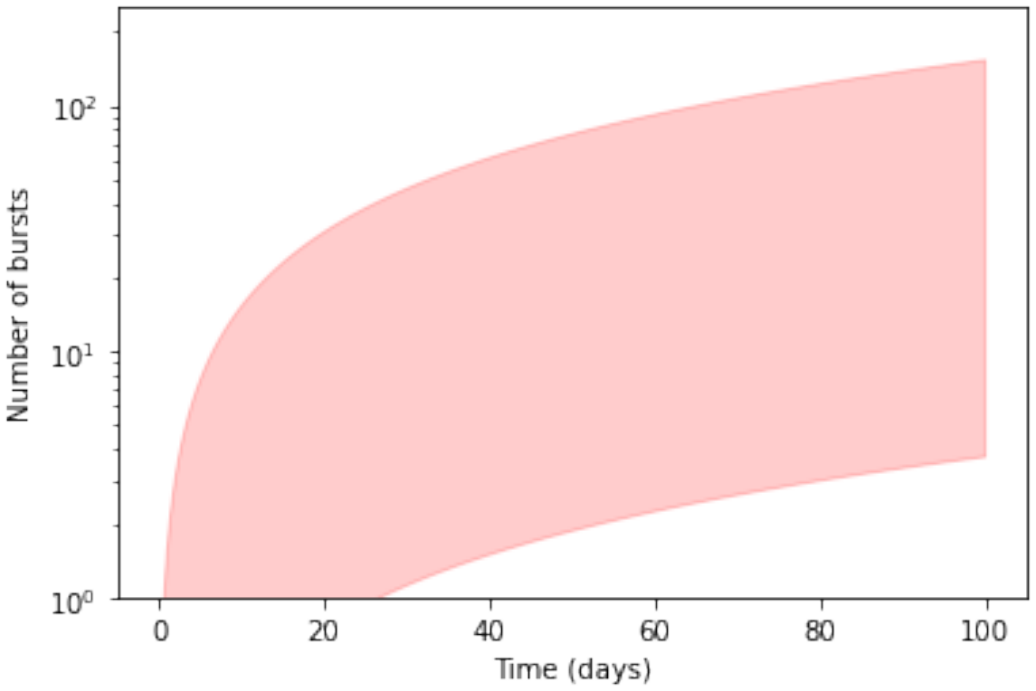

FIGURE 1.7: The likely number of bursts from M82 plotted against time. At a given number of days, the number of FRBs from M82 is anticipated to lie within the shaded region (Hawkins & Lorimer 2021). The shaded region represents the 95% confidence interval for M82 burst rate.

1.2.1 History of Magnetar Bursts

Magnetars are young neutron stars with strong magnetic field strengths. Magnetars must be young neutron stars because their magnetic fields are supported by high levels of rotational energy (Kaspi & Beloborodov 2017). In general, younger neutron stars rotate faster, emitting energy more quickly. As a neutron star's total energy is diminished, the speed of its rotation decreases. Magnetars generally emit radiation over a span of a few thousand years. After that time, the magnetar no longer has enough energy to produce bursts. Because magnetars spin so quickly, they have incredibly strong magnetic fields, up to or exceeding 10^{15} G (Kaspi

& Beloborodov 2017). These magnetic fields provide magnetars with enormous reserves of energy.

Magnetars have a history of producing bursts across the electromagnetic spectrum. In fact, magnetars regularly produce both gamma and x-rays under the names soft-gamma repeaters (SGRs) and anomalous X-ray pulsars (AXPs), respectively (Kaspi & Beloborodov 2017). These bursts vary in luminosity across the electromagnetic spectrum, as well as across time. Bursts in the X-ray band span at least five orders of magnitude. This range of observed luminosities belies the factor of approximately 10 in period and 100 in magnetic field strength observed.

Observers have long suspected that magnetars may produce radio emission. Radio pulsars have been observed to produce magnetar-like activity (Kashiyama & Murase 2017), leading many to theorize that such a relationship may also extend in the other direction.

1.2.2 Galactic Burst

In April 2020, CHIME detected a radio wavelength burst from a Galactic magnetar, SGR 1935+2154 (CHIME/FRB Collaboration et al. 2020). This burst had two sub-burst components, of about 0.585 and 0.335 ms width, respectively. These two components were separated by about 29 ms. The DM of the entire burst is 332.7206 cm^{-3} pc, firmly within the Milky Way. The maximum DM for the Milky Way along the line of sight to the burst is on the order of 500-700 cm^{-3} pc, much larger than the DM of the burst itself (CHIME/FRB Collaboration et al. 2020).

The radio pulse from SGR 1935+2154 was temporally coincident with a hard X-ray/soft γ-ray burst from the source. The X-ray and radio detections are within 3 ms of each other, indicating that they were likely emitted in the course of the same event (CHIME/FRB Collaboration et al. 2020). The detection of X-ray emission coincident with this FRB-like pulse leads many to wonder why FRBs do not generally correspond to sources detected with other multi-wavelength observations.

At the time of this detection, SGR 1935+2154 was in a particularly active phase (CHIME/FRB Collaboration et al. 2020). Hundreds of high-energy bursts were reported during this active phase. However, no other bursts had a radio counterpart. The radio detection corresponds with a brighter high-energy pulse, possibly indicating a minimum energy threshold to emit radio pulses.

Due to the unknown geometry of the source, Bochenek et al. (2020)'s value for the luminosity of SGR 1935+2154 is quoted as a lower limit. The energy released in SGR 1935+2154's radio pulse was 4×10^3 times greater than the most energetic pulse from the Crab Pulsar (previously the brightest Galactic radio burst) (Bochenek et al. 2020). The pulse was also only 30 times less energetic than the weakest extragalactic FRB. This energetic pulse has been deemed FRB 200428, included in the ranks of FRBs, now both Galactic and extragalactic.

1.2.3 M82

Messier 82, or M82, was not found by Charles Messier, but it was included in his famous catalog. M82 is a nearby starburst galaxy, about 12 million light years away. It is the closest starburst galaxy to Earth. M82 has a distinctive elongated shape with a central, dusty bulge, as seen in Figure 1.9. Though spiral arms are not visible in the image, M82 is classified as a spiral galaxy, due to its morphology in near-infrared (Barker et al. 2008). M82 is a member of the M81 Group, meaning that M81 is the gravitational mass that is most influential to M82's motion (Barker et al. 2008).

Starburst galaxies are galaxies that have recently undergone an intense period of star formation. Star formation rate is determined both by spectral analysis of a galaxy and examination of hot star-forming regions. Barker et al. (2008) has determined the star formation rate of M82 largely by determining the number of protostars within a few star-forming regions in M82. Those star forming are packed with very young stars (Kennicutt & De Los Reyes 2021), as well as stellar remnants. These stellar remnants are expected to include magnetars. M82's large population of magnetars make it a particularly good target for FRB study, since

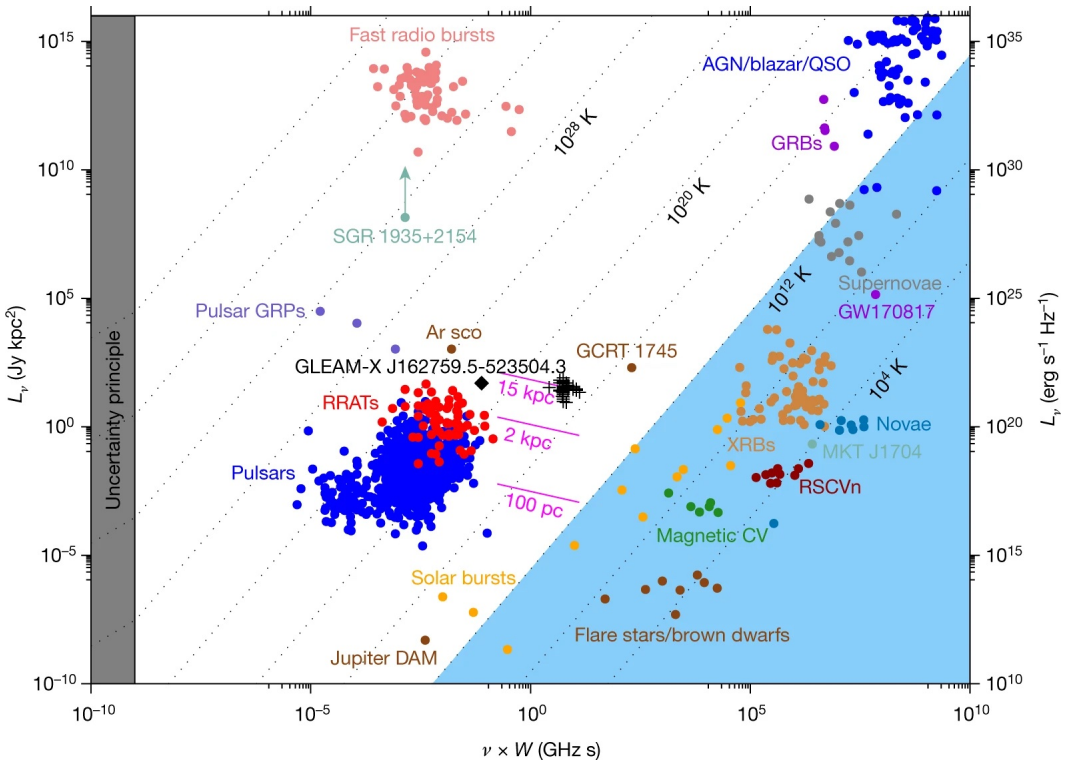

FIGURE 1.8: An overview of transient astronomy. The x-axis represents $\nu \times W$, or the frequency in GHz multiplied by the timescale of the transient. The y-axis shows luminosity. The choice of these axes allows for (dotted) lines of constant blackbody temperature, as indicated. If the energy of a transient event were produced by a blackbody, the temperature contour gives that temperature. FRBs are in the upper left, but SGR 1935+2194 is lower in luminosity than any confirmed FRB, as seen in the upper left. However, SGR 1935+2154 is much brighter than the brightest pulsar. The SGR 1935+2154 detection represents a lower limit on the radio luminosity due to the unknown geometry of the source. It seems likely that SGR 1935+2154 is part of a large population of FRBs that are undetectable due to their greater distances. (Hurley-Walker et al. 2022)

the magnetar hypothesis leads us to expect a higher rate of FRBs from M82 than other galaxies.

1.3 An Overview of this Thesis

In this thesis, I will describe a search for fast radio bursts from the starburst galaxy Messier 82. M82 has a high proportion of magnetars, meaning that it is more likely to emit FRBs, if magnetars are indeed FRB progenitors. If the rate of

FIGURE 1.9: M82 was catalogued by Charles Messier in the 1780s. It is the closest starburst galaxy. Image Credit: NASA

FRBs from M82 is high, that is a good indication that all the relevant assumptions are correct: magnetars are FRB progenitors and M82 contains many magnetars. If the rate of FRBs from M82 is low, that is an indication that at least one of these assumptions is incorrect.

In Chapter 2, I present a review of possible FRB progenitors, with a particular focus on magnetars as progenitors. I begin with cataclysmic progenitors before turning to repeating progenitors.

In Chapter 3, I discuss our data acquisition process: both the measurements and the processing. First, I discuss the telescope used for measurement. Next, I explain the data processing pipeline, with special attention on HEIMDALL and FETCH, two programs used to detect and sort pulses. Finally, I explain the different portions of the data products output by FETCH.

In Chapter 4, I present our results. First, I discuss the candidate population as a whole. Then, I discuss notable bursts and repeating bursts. Finally, I constrain the magnetar burst rate of M82 and discuss our initial assumptions.

In Chapter 5, I present our conclusions. I also discuss future work to be done on the project, including new directions for FRB searches in M82.

CHAPTER 2: FRB Progenitor Theories

Since the discovery of FRBs, astronomers have been formulating theories for their origins. These theories run the gamut from the familiar to the strange to exotic and even alien. At the time of writing, there are over 50 theories in the FRB Theory Wiki[1], a compilation of progenitor theories that have been published in astronomical journals. These theories can be separated into two main categories: cataclysmic and non-cataclysmic progenitors. Simply put, a cataclysmic progenitor destroys itself, meaning that cataclysmic progenitors cannot possibly explain all FRBs. Repeating FRBs require non-cataclysmic progenitors.

The two populations of FRBs lead to more questions: do these two populations arrive from separate progenitors? Are the differences between the two FRB populations due to different conditions in the same category of objects? Do repeating and non-repeating FRBs arise from multiple categories of objects altogether?

While astronomers have considered the possibility that the different populations arise from different progenitors, it is far more likely that the two types come from different conditions in the same kind of progenitor. Because of the similar burst appearances, it is far more likely that repeating and non-repeating FRBs are closely related rather than coincidentally similar. A complete review of the theories for FRB progenitors is outside the scope of this thesis, but some discussion is warranted. In the following sections, I discuss the most popular progenitors of the cataclysmic and non-cataclysmic varieties, focusing on different magnetar progenitors.

2.1 Cataclysmic Progenitors

The first FRB was found in 2007, but the first repeating source was not found until 2016 (Spitler et al. 2016). Because of this nine year time lag, initial theories of FRB progenitors were based primarily on cataclysmic events. After all, there are

[1] https://frbtheorycat.org/index.php/Main_Page

plenty of single burst astrophysical phenomena that arise from destructive events (e.g., supernovae, gamma-ray bursts, etc). Initially, it seemed that FRBs would be added to this list, but evidence has since come to light suggesting that they are more similar to pulsars.

Cataclysmic progenitors come down to two basic scenarios: collisions/mergers or collapses. Most of these involve neutron stars or other compact objects because of their high energy levels. One theory, advanced by Totani (2013), suggests that FRBs are created in binary neutron star mergers. FRBs would be created in the final moments of the neutron stars' inspiral, when their magnetospheres are aligned enough to produce coherent emission (Totani 2013). Earlier in the inspiral, emission would be incoherent, and thus too weak to be detectable. Those final moments, however, should produce a strong radio signal that could be detected as an FRB (Totani 2013). This theory clearly predicts a one-time event. Two neutron stars cannot collide, un-collide, and collide again. In order for this progenitor theory to be valid for all FRBs, they must only originate from galaxies that host neutron stars. Current localizations of FRBs put them in a variety of galaxy types, leading to the downfall of the binary neutron star merger theory's relevance. Though they could still explain some non-repeating sources, they cannot accommodate the whole FRB population. Since most FRBs have not been localized to a particular galaxy, it is difficult to determine the true feasibility of different progenitor theories.

In addition to the merger of binary neutron stars, theorists have proposed neutron star-black hole mergers (Mingarelli et al. 2015), neutron star-white dwarf mergers (Liu 2018), and white dwarf-black hole mergers (Li et al. 2018) as FRB progenitors, as well as several others. However, binary pairs of these types are certainly rarer than current rates of FRBs require, though the rates of such binaries are quite poorly known (Boco et al. 2019).

Many collapse theories of FRB production are also quite popular. A few groups have focused on the collapse of rotating supramassive neutron stars to black holes. Falcke & Rezzolla (2014), Punsly & Bini (2016), and Fuller & Ott (2015) all deal with such scenarios. If a neutron star is rotating rapidly enough, its mass can exceed the maximum mass for a non-rotating neutron star (Falcke & Rezzolla

2014). Such a neutron star can maintain that state as long as the rotation is fast enough to keep collapse at bay. Inevitably, however, a rotating neutron star must lose its rotation due to friction with the surrounding environment (Falcke & Rezzolla 2014). Eventually, the supramassive neutron star will collapse in a very brief time span. A magnetic shock wave would emanate from the collapse and produce radio emission (Falcke & Rezzolla 2014). Fuller & Ott (2015) suggests that this collapse could be induced by dark matter buildup in the core rather than spin down. If a neutron star captures enough dark matter, however it that occurs, Either way, such a collapse would produce a very large energy signature.

There are many other cataclysmic progenitor theories, with a wide range of objects at their focus. Raby (2016) considers axion star-neutron star interactions. Axion stars are stars made of axions, a type of hypothetical exotic matter. Meanwhile, Keane et al. (2012) investigate the evaporation of mini-black holes. Brandenberger et al. (2017) discuss the evaporation of cosmic string cusps as a progenitor theory. Cosmic strings are theoretical objects that were formed in the early universe and stretched to great distances today. Cosmic string cusps are loops of a cosmic string, which can be twisted into ever more complicated formations, trapping energy. Barrau et al. (2014), on the other hand, attribute FRBs to white holes, theoretical exotic objects that are the opposite of black holes: matter and energy come out, but nothing can get in.

2.1.1 Magnetars

Magnetars are young neutron stars with exceptionally large magnetic fields (for a more complete discussion, see Section 1.2.1). Magnetars are currently the most popular theory for FRB progenitors because they are already known to create radio emission, though debate still abounds on the particulars of magnetars as FRB progenitors. One of the first theories for FRB progenitors was a theory involving magnetars.

As early as 2010, astrophysicists proposed magnetar wind shocks as the phenomena that give rise to FRBs (Popov & Postnov 2010). Others built upon this model in following years (see, e.g., Lyubarsky 2014; Murase et al. 2016). In this model,

a magnetar is surrounded by a wind nebula, a shell of gas that had been blown off the neutron star. This material was either ejected in the initial supernova or through subsequent material loss. Any energy that the magnetar releases must collide with the nebula, heating the gas. The heated nebula radiates radio photons to cool down. An FRB would be created when a magnetar hyperflare runs into the surrounding nebula. A magnetar hyperflare is a more intense, and rarer, energy burst from the magnetar. Such a burst arises from instabilities in the magnetic field. As the burst hits the wind nebula, the highly energetic photons (X-rays or γ-rays) are absorbed by the wind particles, eventually leading to the gas radiating radio waves. That radio pulse could be quite energetic, leading to FRBs. The problem with such a model is that it cannot answer the question of all repeaters. Such energy could not be produced by a magnetar at the timescales of many repeaters (often multiple bursts in an hour) (Murase et al. 2016).

2.2 Repeating Progenitors

After Spitler et al. (2016) confirmed FRB 121102 was a repeating source, theorists suddenly had to account for high energy bursts without destruction of the source. Models that encompassed all FRBs must be non-cataclysmic, though some groups continued working on cataclysmic models, in case FRBs arise from different sources. Mergers and collisions are necessarily cataclysmic, but neutron stars continue to dominate the landscape of repeating FRB progenitors.

Ghisellini (2017) suggest that FRBs are created in synchrotron masers around neutron stars. A synchrotron maser is a particular mechanism that focuses energy into a more coherent structure, resulting in stronger and more easily detectable radiation. Synchrotron emission takes place in highly magnetized environments. Neutron stars are highly magnetized, even if they aren't magnetars. Particles released from the surface of the magnetic field are accelerated in spirals along those magnetic field lines, they produce radio emission in the form of an FRB. If the particles being accelerated are electrons, the magnetic field can be quite small (10-100 G) (Ghisellini 2017). However, in order for such a maser to produce a visible burst with electrons, it must be quite close. Since FRBs are confirmed

extragalactic sources, the accelerated particles must be protons instead, requiring a much larger magnetic field (10^4-10^5 G) (Ghisellini 2017). These magnetic fields are much lower than those of most magnetars, however. Many magnetars have magnetic fields in the range of 10^{12}-10^{14} G (Kaspi & Beloborodov 2017). Metzger et al. (2019) continued work on this theory, explaining how repeated bursts in close succession would drift downward in frequency, as discussed in Petroff et al. (2021).

While most neutron star theories focus on magnetars, Kashiyama & Murase (2017) consider the possibility that FRBs are rotation powered, so the neutron star need not have a particularly high magnetic field. In such a model, a neutron star rotates quickly enough to accelerate particles off its surface at sufficient speed. Neutron stars need to be quite young to have the requisite energy to accelerate particles. Only neutron stars in the first stages of their lifetimes have enough energy. As they age, neutron stars lose energy due to friction with surrounding particles and the loss of energy through radiation. After a neutron star's period has lengthened too far, the rotation can no longer power FRBs.

There are many other repeating progenitor theories, ranging from familiar to more exotic ideas. On the most pedestrian side, Geng & Huang (2015) discuss asteroids and other small bodies falling onto neutron stars. Dai et al. (2016) also theorize that FRBs are created in collisions between neutron stars and asteroids. Some neutron stars may collide with a stellar system with an asteroid belt. As those asteroids happen to collide with the surface of the neutron star, energetic bursts are produced: FRBs. Cordes & Wasserman (2016) theorize that FRBs are particularly interesting giant pulses from young pulsars. Katz (2017) considers the possibility that FRBs arise from pulsar lightning, or the release of electrostatic energy in pulsars. Other groups keep their theories within the realm of neutron stars. Gu et al. (2016) develop a model of FRBs coming from neutron star-white dwarf accretion. In a binary pair, the white dwarf may eject material that falls onto the neutron star. As this process takes place, complicated interactions between the two objects' magnetic fields cause reconnection, leading to a burst of radiation. On the most exotic end of the spectrum, Lingam & Loeb (2017) suggests that FRBs could be attributed to beams powering alien light sails. Light sails power spacecraft by absorbing the momentum of beamed photons to travel in that direction, similar

to the way that wind propels a sailing ship. While alien light sails are a somewhat ridiculous solution to the FRB progenitor problem, they are still fun to ponder.

2.2.1 Magnetars

Like cataclysmic progenitors, the repeating FRB progenitor landscape is dominated by magnetars. After all, neutron stars are relatively abundant. It stands to reason that some fraction of them would have large magnetic fields, thus classified as magnetars. There are many different theories for how exactly magnetars produce FRBs.

Metzger et al. (2017) theorize that FRBs are connected with magnetar births. Magnetars form after a massive star (between 10 and 25 $M_{\odot}$) has undergone a core-collapse supernova. Such stars must also have high magnetic fields. After the magnetar has reached a stable state, it is rotating more slowly than before, but still with a maximum period of only a few seconds. Magnetars must initially have millisecond rotation periods to produce strong magnetic fields (Metzger et al. 2017). A magnetar with a fast period will be magnetically braked as it ages, lengthening the period and strengthening the magnetic field. As a magnetar continues to evolve, its period gets longer. When a magnetar is quite young, however, it is spinning rapidly, creating a lot of energy. The magnetar also has a store of residual energy from its collapse. The excess energy can be released in a rapid series of pulses, as observed in many repeating FRBs. Such magnetars must be in the first decades of their lives.

Beloborodov (2017) considers FRBs arising from a synchrotron maser at the termination shock of a magnetar wind nebula. A magnetar wind nebula is a spherical shell of gas that has been ejected from the magnetar. This material surrounds the magnetar and is hit by any energy leaving the magnetar's surface. The termination shock of such a nebula is the edge of the nebula where gas absorbs outgoing energy. This gas is ionized and begins to radiate energy to lower its overall energy state and temperature. There must be a huge amount of power to create FRBs in such a manner (Beloborodov 2017). If the energy is less intense, the Doppler shift of the emission would be larger than that observed in FRBs. However, energies

cannot be so high that they "exhaust" the termination shock (Beloborodov 2017). If the gas has not sufficiently cooled, it cannot produce another burst of energy as magnetar emission hits the shock line. Gas needs to be heated quickly in order to produce energy in a maser, so it must cool below a certain threshold to absorb enough energy to produce this effect. Repeating bursts of FRBs occur in quick succession, so the energy must be low enough to allow for cooling. Such repeating FRBs may be quite rare due to the stringent constraints on such a system, though they would have the ability to produce a large number of bursts in a relatively short time (Beloborodov 2017).

Katz (2016) postulates that FRBs are created by arches of magnetospheric current, like the arches of a star's corona. Those arches could have long lifetimes, on the order of thousands of years at the longest (Katz 2016). Currents moving along those arches could carry large energies which would then be released by plasma instabilities within the arches themselves. Alternatively, energy could be released by the movement of arches according to shifts in the magnetar crust. As pieces of the neutron crust move, different portions of the magnetar's interior are exposed, leading to changing magnetic field profiles. When a current is displaced by the movement of magnetic field lines, an FRB is produced (Katz 2016). On the other hand, FRBs could be produced by curvature radiation caused by the clumping of charged particles on the magnetic arches. Curvature radiation is produced when charged particles move at relativistic speeds along a curved path of a magnetic field. One problem with curvature radiation is that such signatures would be more likely to occur at higher frequencies than those of FRBs.

CHAPTER 3: Data Sources & Processing

Our data was gathered by the 20 meter telescope at Green Bank Observatory. Over a period of slightly over a year, from October 2020 to January 2022, we scheduled observations of a maximum of ten hours. At the end of the project, we have a total of 28.2 days of on-source time on M82. All of that data was sent through automated processing pipelines, HEIMDALL (Barsdell et al. 2012) and FETCH (Agarwal et al. 2020), where bursts were located and then sorted into source and interference. In Section 3.3, I show an example data output and explain the different portions of the image.

3.1 Data Sources

The Green Bank Observatory (GBO) is an excellent place to gather radio data because it is located in the radio quiet zone in West Virginia. The radio quiet zone includes portions of West Virginia, Virginia, and Maryland, where radio transmissions are heavily restricted. These restrictions allow GBO to collect observations with a much lower level of human-made radio interference.

The 20 meter telescope at GBO was built by the US Naval Observatory in 1994[1]. The telescope is shown in Figure 3.1. The Navy gave the telescope to GBO in 2000. Since 2008, this telescope has been used by students and other small projects. Researchers can apply for telescope time using the Skynet Robotic Telescope Network. The list of our observing times is shown in Appendix A. In our project, we used the L-band receiver, which has a bandwidth of 125 MHz centered at 1.4 GHz. The L-band contains the rest frequency of the neutral hydrogen spin flip and is a commonly used radio waveband. While this specific transition does not occur in FRBs, the frequency coverage of the L-band is a good window onto radio phenomena of all kinds.

[1] https://greenbankobservatory.org/science/telescopes/20m

FIGURE 3.1: The 20 meter telescope at Green Bank Observatory. Image Credit: Green Bank Observatory

The specific 125 MHz window was chosen to minimize noise and interference while maximizing signal. Outside of this frequency range, interference becomes a larger problem. The 125 MHz window is split into 256 channels. In order for the algorithms described further in this chapter to function, the number of channels must be a power of two. The best signal-to-noise ratio occurs in an even smaller window, the 80 MHz between ∼1360-1440. This window is considered the 'usable bandwidth' with the greatest concentration of signal. These bandwidths and other important system values are given in Table 3.1.

After the L-band receiver registers signal, that signal is amplified and filtered. The filters impose the bandpass on the data. Any data that does not fit the bandpass are removed by the filters. The data is then sent through an analog to digital converter, which changes the analog signals of the telescope to digital signals that can be processed by a computer. From there, data are configured to their final form and saved on a local disk. Those files are then sent to HEIMDALL and FETCH, the programs we used to find and sort candidate pulses, discussed in detail in Sections 3.2.1 and 3.2.2. The pipeline is shown schematically in Figure 3.2.

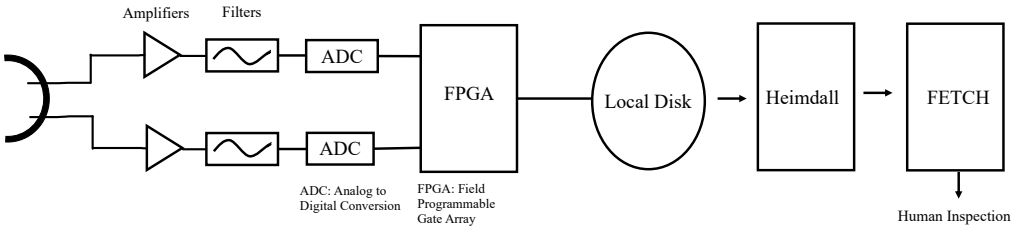

FIGURE 3.2: Schematic of the data acquisition and analysis pipeline, from the receiver to the final data outputs.

Parameter	Value	Units
Telescope gain, G	0.086	K Jy^{-1}
Total bandwidth, $\Delta\nu$	125	MHz
Usable bandwidth, $\Delta\nu$	80	MHz
Number of channels, n	256	
Channel bandwidth, $\Delta\nu_{\rm chan}$	0.488	MHz
System temperature, $T_{\rm sys}$	40	K
Center frequency, ν_0	1.4	MHz
Sampling interval, $t_{\rm samp}$	131.07	μs

TABLE 3.1: System values for the 20 m telescope at Green Bank Observatory. The usable bandwidth represents the portion of the total bandwidth that has the best signal-to-noise ratio.

3.2 Data Processing

Astronomical surveys generate huge amounts of data, given their hundreds of hours of observing time. It is impossible for a single person, or even a team, to process such a huge amount of data in a timely manner. Transient searches in particular generally result in at least 10^4 candidates per hour, which is far too many to be reviewed by eye (Barsdell et al. 2012). And those candidates have already been passed through intense data processing. In short, it is not possible

for researchers to process and sort data by hand, so they must rely on computer processes and algorithms. In this project, we used two algorithms to process our data. HEIMDALL handles initial dedispersion over frequency and time and carries out detection of individual pulses in the data, while FETCH uses artificial intelligence to select the best pulses.

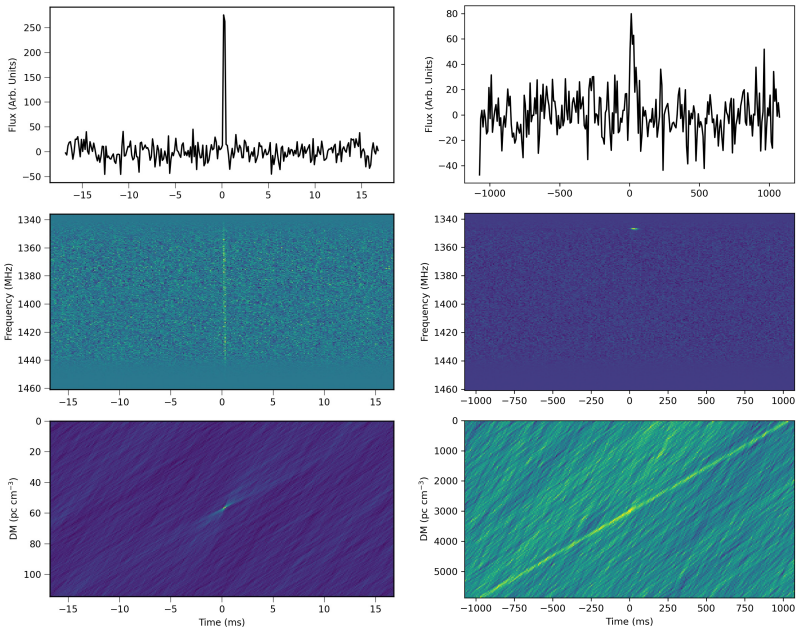

FIGURE 3.3: This figure shows the difference between an astrophysical pulse, on the left, and radio frequency interference (RFI), on the right. RFI has a line through the DM panel rather than a single peak and a smaller frequency range than that of an astrophysical burst. Specific discussion of the panels is given in Section 3.3.

FETCH is able to sort out good pulses from the bad. A major issue in radio astronomy is the presence of radio frequency interference (RFI) in data sets. RFI can be caused by any human source of radio waves: microwaves, cell phones, cameras, airplanes, radar, etc. While the Green Bank Observatory (GBO) engineers have done as much as they can to lower RFI, there are still sources sneaking in every day. RFI often takes a similar shape to astronomical pulses, so FETCH's ability to identify RFI is critical. Figure 3.3 shows a sample source pulse and RFI pulse to show the differences between the two, as well as their similarities.

3.2.1 HEIMDALL

The HEIMDALL[2] algorithm was developed by Barsdell et al. (2012). HEIMDALL is a dedispersion algorithm with GPU acceleration. It requires data with both high time and high frequency resolution. Because FRBs have been dispersed by their travel through intergalactic and interstellar space, that dispersion needs to be corrected in order to find bursts. HEIMDALL dedisperses possible signals by correcting for frequency dependent time delay, given in Equation 1.1.

HEIMDALL chooses a value of DM and a value of ν_1 and uses Equation 1.1 to determine the time delay for each frequency. The algorithm can then sum the power across these frequencies. If an excess of power, with a signal-to-noise ratio of at least 10, is found in one combination of DM and time sample, an astrophysical pulse was emitted. HEIMDALL repeats this process for many different values of DM and different sized time bins.

HEIMDALL takes the thousands of time series it has created and searches them for bursts. The burst detection process begins by convolving a given time series with a box-car of some width (Barsdell et al. 2012). The first layer of convolution has a fairly large kernel, intended to capture broader pulse widths. HEIMDALL then uses progressively smaller kernels to detect signals and fine tune possible structure. Only the bursts with a S/N greater than 6 are considered viable candidates and sent onward. The S/N ratio is determined by the relative strength of the burst detection and the general noise level. After HEIMDALL has finalized its burst determinations, those bursts are sent to a small secondary program to produce images that FETCH can analyze.

3.2.2 FETCH

After HEIMDALL has found bursts, FETCH must categorize those bursts. There could be thousands of burst candidates found in an hour, and a computer is necessary to sort through such a high number of candidates. FETCH is a neural network with a process shown in Figure 3.4. A neural network is a computer

[2]https://sourceforge.net/projects/heimdall-astro

program that recognizes connections underlying large sets of data. The input layer represents the user's inputs, in this case the outputs of HEIMDALL (Agarwal et al. 2020). Then, there are convolution layers, where the network compares new images with an understood catalog. FETCH uses many image convolution layers. In the dense layer, different features of a particular burst are assigned likelihoods of belonging to different catergories (e.g. RFI, pulsar, or FRB) (Agarwal et al. 2020). The candidates labelled as pulsars or FRBs are sent to an output layer, where they can be saved in a folder for a researcher to look over. Those outputs are shown in Section 3.3.

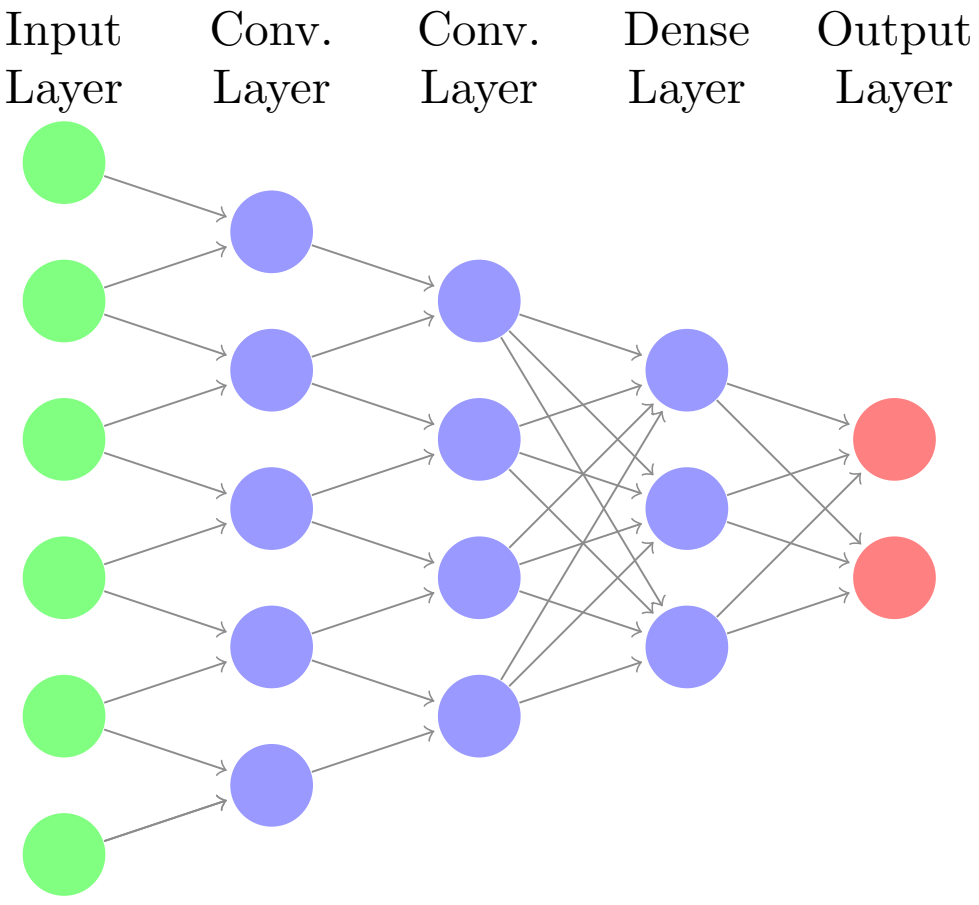

FIGURE 3.4: The FETCH algorithmic process, as described in this section, is represented in this image. The different layers have different functions that combine to form a cohesive set of results. (Agarwal et al. 2020)

FETCH has been tested extensively. In test sets, it identified all pulsars and FRBs correctly, and only misidentified a few RFI pulses (Agarwal et al. 2020). There are several versions of FETCH, each with different parameters for kernels,

convolution layers, and sorting criteria. Each version of FETCH has an accuracy of over 99%, with the lowest accuracy at 99.66%. Most of the inaccuracies come from misidentification of RFI. FETCH is crucial to the research because of its ability to find and sort pulses much faster than any human can. The candidates that FETCH deems real signal are collected and must then be checked by researchers.

3.3 Example Outputs

HEIMDALL outputs images like those in Figure 3.5 below. All the images that are considered scientifically useful have been sorted into a science category by FETCH. These figures show the dedispersed pulse (top), dedispersed frequency versus time (middle), and the search for the pulse in DM space. The typical time range shown in these figure is on the order of tens of milliseconds, while the bursts themselves are generally a few milliseconds long.

The burst shown below is from the Crab Pulsar, a young pulsar with a period of 33 ms in the Crab Nebula (Comella et al. 1969). It is an extraordinarily bright pulsar close to Earth. The Crab's pulses can be easily detected (Staelin & Reifenstein 1968) (and indeed the Crab was originally discovered through its bright individual pulses), and they have very high signal to noise ratios. Crab pulses are the ideal testing ground for radio burst detection. The ideal features of a radio pulse are very easy to see in an image from the Crab Pulsar.

The top panel of Figure 3.5 shows intensity versus dedispersed flux and time. The zero point on the time axis indicates the time of the burst, as determined by HEIMDALL. The time axis then shows time before and after the burst in milliseconds. The flux in the top panel has been dedispersed to allow for burst detection. Because of the time spread of a dispersed burst, it is much more difficult to detect a burst that has not been corrected for dispersion. HEIMDALL's algorithm dedisperses bursts before it begins the detection process. The top panel shows that dedispersed burst, which towers above the noise level of the image. The candidate pulses from M82 reported in this work are much closer to the noise level than this Crab pulse.

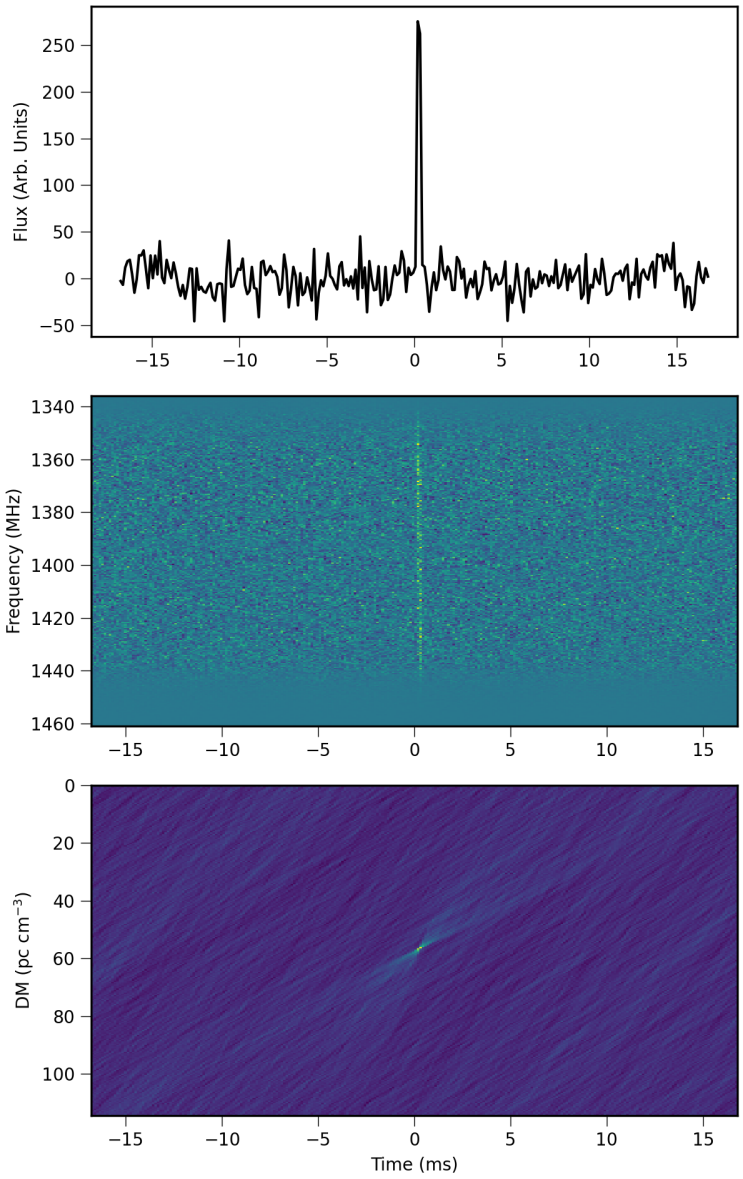

FIGURE 3.5: A sample pulse from the Crab Pulsar. The top panel shows dedispersed flux versus time, the middle panel shows intensity versus dedispersed frequency and time, and the bottom panel shows DM versus time. This particular burst has a DM of 57.17 cm^{-3} pc and a signal-to-noise ratio of 25.21.

The middle panel of Figure 3.5 shows the dedispersed frequency versus time. HEIMDALL has determined a usable frequency band of about 80 MHz, from 1360-1440. This band includes 1420 MHz, the frequency of the hydrogen spin-flip transition for neutral hydrogen. The dedispersed frequency should be a vertical line at the zero mark of the time axis. When HEIMDALL dedisperses a time series, all the flux of a particular burst should be visible at one point in time.

The intensity of the frequency detection is shown by the color of the pixels. Yellow indicates more power at that location in phase space, while dark blue is the lowest power. Most astrophysical bursts have a vertical line through the whole bandwidth centered at 0 ms. If a burst only has flux at a single frequency, that indicates probable RFI.

The bottom panel of Figure 3.5 shows the dispersion measure (DM) versus time. The DM panel indicates the best DM for a particular burst. There should be a peak in the DM panel, indicating the dispersion measure for that particular burst. This DM represents the value that HEIMDALL has determined best fits the data. There is a small range of DM values that could fit the data to varying degrees of success. The most successful DM at the time of the burst is brightest green, while other values decrease into the blue. This Crab pulse has a DM of about 57 cm^{-3} pc, represented by the bright green peak on the dark blue background.

CHAPTER 4: Results

After visually inspecting each of the 291 output files FETCH determined as viable, I selected 27 of the best candidates from ∼75 good candidates. These candidates were determined based on the sharpness of the peak in DM-space, the clarity of the line in the dedispersed frequency panel, and the dominance of the peak in the dedispersed flux. Ideally bursts would look like the example Crab pulse (Figure 3.5). However, none of these candidates are that clear. Good candidates are defined as those with visible features. The best candidates are listed in Table 4.1 and shown in Appendix B.

In Table 4.1, the first column is the Modified Julian Date (MJD) of the observation. The MJD represents the time of the observation given in the number of days since midnight on November 17, 1858. The second column gives the DM in units of cm^{-3} pc. Next comes pulse width in units of ms and flux density in units of Jy. Finally, the S/N is given. The S/N is determined by HEIMDALL.

None of the bursts have a particularly high signal-to-noise ratio: the highest is 7.5. Unfortunately, the S/N threshold to be certain of a detection as an FRB is about 10, meaning that none of these bursts are quite bright enough to be definitive. Since HEIMDALL runs tens of thousands of trials per burst, a higher S/N ratio is needed to represent a statistically significant detection. The threshold of 10 is high enough that any bursts with that S/N are sure to be genuine astrophysical signals. Nonetheless, these bursts remain compelling, particularly those with high DMs. Higher DMs are more likely to be extragalactic, as bursts must travel further, and thus through more free electrons. Extragalactic DMs include the contribution from the Milky Way, as well as the contributions from intergalactic space and their host galactic medium. All of the 27 selected bursts have DMs that are larger than the DM values expected from the Milky Way along this line of sight (~ 30 cm^{-3} pc) Cordes & Lazio (2002).

Though none of the candidate bursts from M82 have a high enough S/N to be considered an FRB, I have plotted their flux densities, pulse widths, and dispersion measures against those of confirmed FRBs. These candidates have fairly average

Observation MJD	DM (cm^{-3} pc)	Pulse Width (ms)	Flux Density (Jy)	S/N
59135.77	337.56	2.09	4.92	6.13
59140.26	1177.59	4.19	3.65	6.44
59150.63	210.43	1.05	6.95	6.12
59168.67	1549.58	8.39	2.52	6.27
59168.67	144.42	1.05	7.24	6.38
59176.03	79.74	0.26	15.69	6.91
59176.03	108.55	1.05	7.03	6.19
59184.21	4044.03	8.39	2.61	6.50
59192.48	92.84	0.52	10.14	6.31
59193.17	2712.07	8.39	2.98	7.42
59235.03	815.98	4.19	3.68	6.48
59240.67	1446.85	4.19	3.91	6.88
59307.81	113.52	0.52	9.72	6.06
59307.81	3040.06	16.78	1.88	6.62
59330.54	496.83	2.10	5.95	7.41
59485.58	98.97	0.52	10.16	6.33
59485.58	727.37	2.10	5.43	6.76
59488.06	158.65	0.52	10.22	6.36
59489.00	183.10	0.52	10.36	6.45
59496.39	1305.33	4.19	3.80	6.70
59507.00	110.19	0.52	10.37	6.45
59507.00	127.46	1.04	6.94	6.11
59514.62	275.54	1.04	8.52	7.50
59515.16	384.31	2.10	5.30	6.60
59517.17	169.43	1.04	7.62	6.71
59521.61	362.35	2.10	4.95	6.17
59536.52	663.37	2.10	5.32	6.63

TABLE 4.1: Best FRB Candidate Observations

pulse widths (seen in Figure 4.1) compared to those of confirmed FRBs. Some of the pulse widths are short compared to most FRBs, but the majority of the candidates have a pulse width that falls in the main body of known FRBs' pulse widths. The candidates' pulse widths follow a periodic pattern because FETCH calculates the pulse width by determining a number of time bins in which a pulse is visible. These bins are set by a sampling time (1.3×10^{-4} s), meaning that FETCH can only determine pulse widths that are multiples of this sampling time. This sampling time is linked to inherent systematic limitations of the 20m telescope and is therefore a limitation of this work.

The candidate bursts also have flux densities that are slightly higher than the

majority of FRBs, but nothing too high. The 20 meter telescope is not nearly as sensitive as a telescope like CHIME, due to its smaller size. However, we are able to detect pulses with a flux density on a similar scale to those of known FRBs.

We determine flux density using the radiometer equation,

$$S = \frac{(S/N)\,T}{G\sqrt{2BW}}, \tag{4.1}$$

where S is the flux density, S/N is the signal-to-noise ratio, T is the system temperature, G is the telescope gain, B is the bandwidth, and W is the pulse width. For this particular system, $T = 40$K, $G = 0.086$ K/Jy, and $B = 80$ MHz. W is determined by multiplied the sampling time by the number of time bins in which source is detectable.

The relationship between pulse width and flux density in Figure 4.1 is very close to linear. The linearity of the line likely indicates that these pulses are noise. In a set of real pulses, there would be greater spread in the S/N, leading to a more complicated relationship between pulse width and flux density.

The candidate bursts' DMs span a range slightly greater than that of known FRBs (as shown in Figure 4.2). A couple of the bursts have very low DMs, around 50 cm^{-3} pc. If real, these bursts may be within the halo of Milky Way in this line of sight, given their low DMs. The highest DMs from this candidate group are a bit higher than known FRBs. The highest DM is about 4,000 cm^{-3} pc (see Table 4.1). While this value is higher than the highest DM of a known FRB, 3037.7 cm^{-3} pc for FRB180906B (Spanakis-Misirlis 2021), it is within the same order of magnitude, certainly a possible value for DM. The DM within M82 is still unknown, but it is unlikely that it would be so high, especially compared to the DMs of the other candidates. The DM values for M82 are relatively unknown, but reasonable values lie somewhat around the range of 75-500 cm^{-3} pc, consistent with what is known from pulsars in our galaxy.

In the following sections, I will discuss specific candidate bursts, as well as repeating DM values throughout the data set. I will finish with a calculation of the FRB rate from M82 and the ensuing implications.

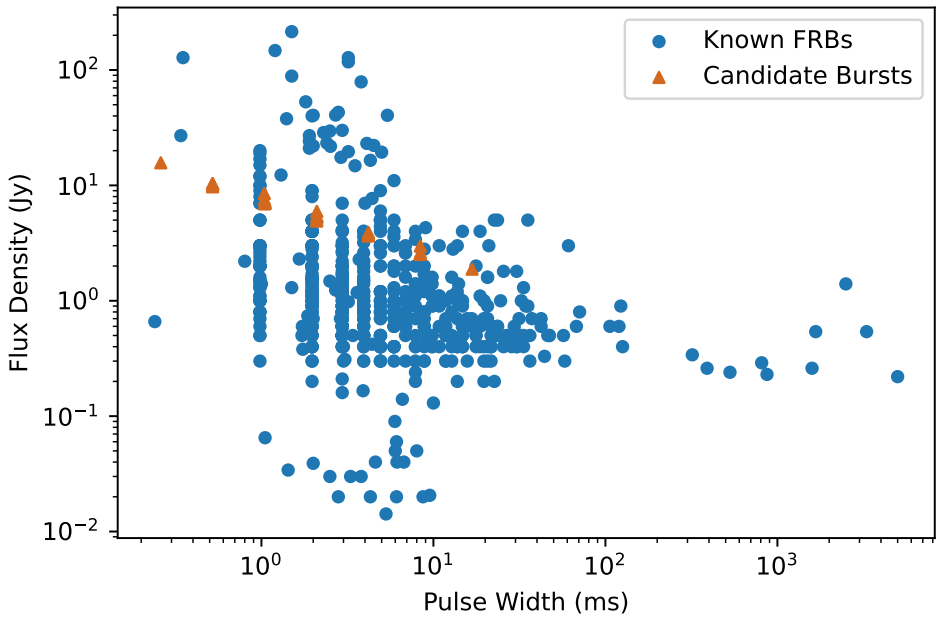

FIGURE 4.1: The pulse width plotted against the flux density for both known FRBs and the candidate pulses from M82. Known FRBs are in blue and M82 candidate pulses are in purple. The linear structure is an indication that these candidates are likely noise. If they were real pulses, there would be greater spread in the flux density.

4.1 A Few Representative Bursts

Four bursts from the list of the best candidates are discussed in this section. They are shown in Figures 4.3, 4.4, 4.5, and 4.6. These candidates are emblematic of the entire sample set. They are much fainter than the Crab pulse shown in Section 3.3, but the same features are present. Each of these candidates has a clear peak in dedispersed flux, centered at zero. They also have a vertical line through the entire dedispersed frequency range. Finally, they have a peak in DM-space, indicating that this data is only well matched by one DM. Radio frequency interference (RFI) will often fit with many values of DM, due to the differing nature of the sources, as shown in the bottom panel of Figure 3.3. Many human sources of radio waves broadcast at multiple frequencies simultaneously, which means that multiple DMs can fit the same set of data. When there is a single peak in the search for DM, that is an excellent indicator that the source is probably astrophysical in nature. Each

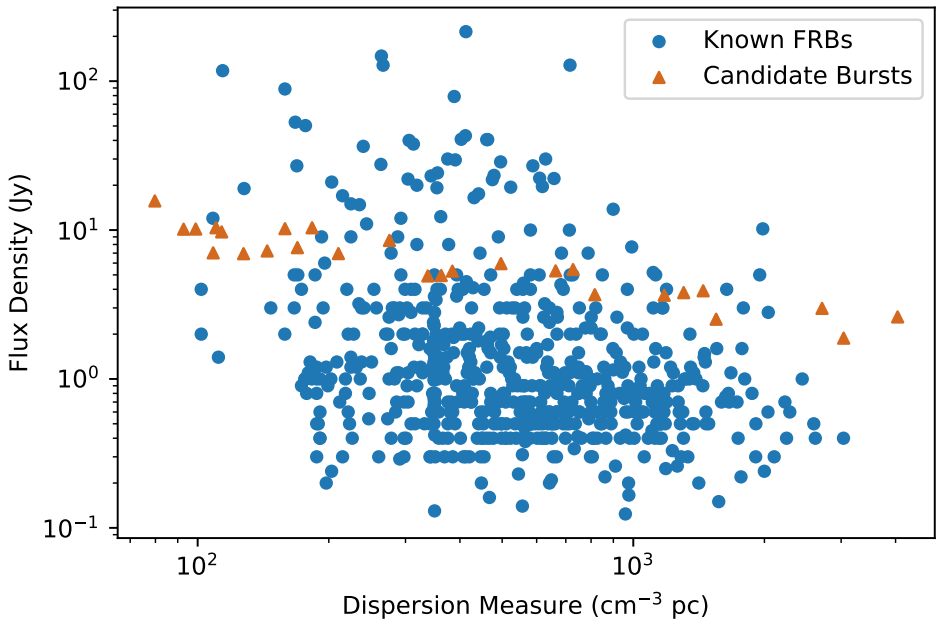

FIGURE 4.2: The flux density plotted against the dispersion measure for both known FRBs and the candidate pulses from M82. Known FRBs are in blue and M82 candidate pulses are in purple.

candidate is given a candidate number and an observation number from FETCH. The observation number is the Modified Julian Date (MJD) for the beginning of the observation. The candidate number represents the amount of time that has elapsed since the beginning of the observation, in seconds. For example, Candidate 59168.67_15033.1 was found 15033.1 seconds after the beginning of the observation at 59168.67.

The first candidate to discuss is Candidate 59168.67_15033.1, shown in Figure 4.3. Candidate 59168.67_15033.1 has a S/N of 6.38, but the pulse still jumps out in the dedispersed flux panel. There is a vertical line down the center of the dedispersed frequency panel, indicating that the burst took place at multiple frequencies simultaneously. Finally, the DM panel shows a peak in the center, indicating that there is a particular DM that best matches the data. The DM itself is 144.42 cm^{-3} pc, consistent with an origin in M82. The pulse width is only 1.05 ms, which is quite short for an FRB. The flux density is 7.24 Jy, a normal value for an FRB.

The next candidate is Candidate 59330.54_6537.1, shown in Figure 4.4. It has a

S/N of 7.41, which is on the higher end of this data set. This S/N is still too low to be a definitive detection, though. Despite the higher S/N, the peak of the dedispersed flux panel is visually less distinctive than the peak of Candidate 59168.67_15033.1. Candidate 59330.54_6537.1 also has a fainter dedispersed frequency line. The DM is still visible and somewhat strong, with a value of 496.83 cm^{-3} pc. The pulse width is 2.1 ms, twice as long as the width of Candidate 59168.67_15033.1 and an average width for known FRBs. The flux density is only 5.95 Jy, which is somewhat low.

The next burst is Candidate 59496.39_2560.0, shown in Figure 4.5, with a S/N of 6.7. The peak in the dedispersed flux panel is distinctive, and the vertical line in the frequency panel is more visible than that of Candidate 59330.54_6537.1. The peak in the DM panel is also quite distinctive, with a value of 1305.33 cm^{-3} pc, considerably higher than expected from M82. Such a DM value would higly depend on a large component from M82 itself, perhaps larger than reasonable. The pulse width is 4.19 ms, which puts it in the average length of the FRB population. The flux density is only 3.8 Jy, making it a bit dimmer than the previous example bursts.

Finally, Candidate 59536.52_7801.27, shown in Figure 4.6, has a S/N of 6.63. The peak in the dedispersed flux panel looks wider than the peaks of previous candidates, and there are slightly higher peaks in the noise. Nevertheless, the vertical line in the dedispersed frequency panel is clear, and the peak in the DM panel is also clear. The DM value is 663.37 cm^{-3} pc, putting the candidate in the extragalactic range. Candidate 59536.52_7801.27 has a pulse width of 2.1 ms, like Candidate 59330.54_6537.1. It also has a similar flux density of 5.32 Jy.

4.1.1 Repeating DMs

Due to the prevalence of repeating FRBs, it is vital to check the collection of candidates from M82 for repeating DMs. I determined that there are two DMs that have an unusual number of repetitions: four. Many of the DMs are repeated two or three times, but only two DM values have four bursts each. These DMs are 719.052 cm^{-3} pc and 215.746 cm^{-3} pc.

The bursts with 719.052 cm^{-3} pc (shown in Figure 4.7) are less clear than the bursts sorted into the best category in the previous section. Despite this, three of the four bursts are quite clear, though the other is closer to the noise level. In Figure 4.7, this burst is the second from the left. These four bursts are Candidates 59142.61_16874.6, 59147.00_7096.96, 59173.77_16727.8, and 59207.85_5467.62. The physical characteristics of any of these single bursts are not remarkable, due to their similarity to the other candidates. Each pulse has a peak in flux as well as a dim line in frequency space and a faint peak in DM space. The shared DM is more interesting than the individual characteristics of these bursts.

The bursts with 215.746 cm^{-3} pc (shown in Figure 4.8) are clearer than those with 719.052 cm^{-3} pc. All four of these bursts have a vertical line in dedispersed frequency space, as well as peaks in DM space. The candidates are 59144.11_15684.3, 59165.08_9778.94, 59486.00_4326.89, and 59516.17_4014.06. These four bursts are all similar to the other candidates found in the search. While none of them are bright enough to be confirmed as FRBs, the data are still quite good. Following Hawkins & Lorimer (2021), we can determine the significance level of finding n bursts within a single DM trial as

$$C = \sum_{i=0}^{n-1} \frac{(N/T)^i \exp(-N/T)}{i!}, \tag{4.2}$$

where N is the total number of bursts, and T is the number of trial DM used by HEIMDALL. For $n = 4$ bursts from a sample of $N = 291$ pulses with $T = 462$ DM trials, we find $C = 99.6\%$.

While the above confidence level is marginally significant, unfortunately, we would need a higher number of bursts in a single DM. In order to achieve a confidence level of 5σ, the gold standard for scientific discoveries, we would need to find at least 8 bursts with the same DM. A confidence level of 5σ results in a C of 99.99994%. Neither of the repeating DMs have a large enough number of bursts to be considered a 5σ detection.

4.2 Constraining the Magnetar Burst Rate of M82

Since none of the candidate bursts can be officially classified as an FRB, the initial hypothesis of this study is invalid. By day 28, we expected to have found at least one FRB (see Figure 1.7). Without a detected burst, we must reexamine our assumptions to draw new conclusions.

The rate of FRBs from M82 must be less than $1/28.2$ day^{-1} $= 0.035$ day^{-1}. If the rate were any greater, an FRB would have been detected by now. We can use this rate to find a relative star formation rate for M82, based on the data from Bochenek et al. (2020) where the rate of magnetar bursts was found to be R_{STARE2}. We can express this condition as

$$\frac{\mathrm{SFR_{M82}}}{\mathrm{SFR_{MW}}} = \frac{\mathrm{RFRB_{M82}}}{\mathrm{R_{STARE2}}}, \tag{4.3}$$

where $\mathrm{SFR_{M82}}$ is the star formation rate of M82, $\mathrm{SFR_{MW}}$ is the star formation rate of the Milky Way, and $\mathrm{RFRB_{M82}}$ is the FRB rate of M82. The lower limit of R_{STARE2} is 3.6 yr^{-1}, which I'll use in this calculation, since our FRB rate is below the lower end of our distribution. With this rate and $\frac{\mathrm{SFR_{M82}}}{\mathrm{SFR_{MW}}} = 40$, the FRB rate of M82 is less than 3.6, further meaning that the star formation rate of M82 must be less than 3.6 times that of the Milky Way, assuming that FRB rate scales with star formation rate. This rate blatantly contradicts Barker et al. (2008), who find $\frac{\mathrm{SFR_{M82}}}{\mathrm{SFR_{MW}}} = 40$.

The incompatibility between these two values confirms that this project's initial assumption, that magnetar burst rate scales with star formation rate, is incorrect. There are a few possible explanations for this discrepancy. Possibly, M82 contains fewer magnetars than expected, or those magnetars are less active than the Milky Way population. Perhaps M82's starbursting environment suppresses magnetar bursting. It is also possible that not all FRBs arise from magnetars. If magnetar bursts only make up a small fraction of the FRB population, our results are consistent. Our results are not solid enough to do anything mroe than speculate. All

we know for certain is that, if we assume that all FRBs arise from magnetars, our results prove that magnetar burst rate does not scale with star formation rate.

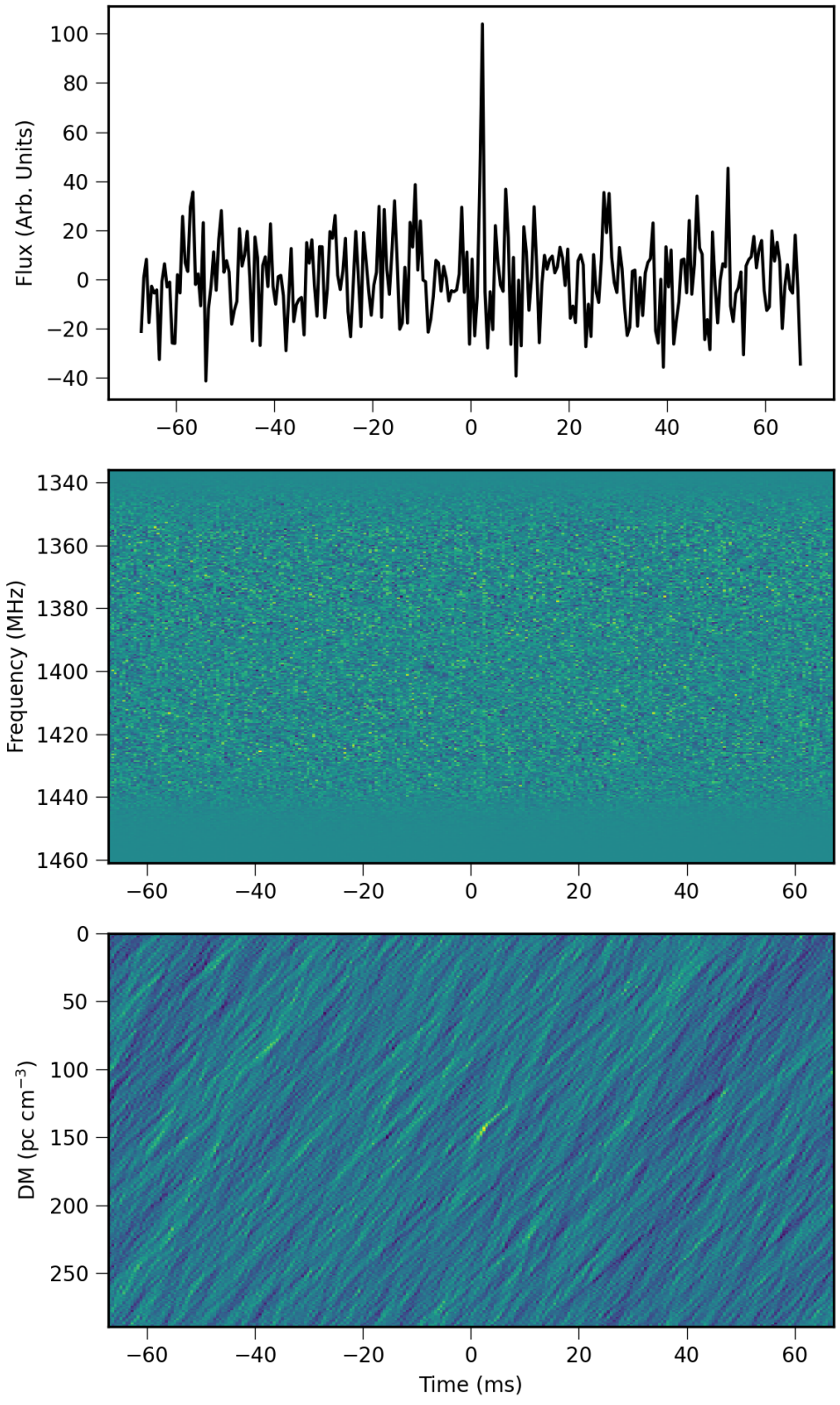

FIGURE 4.3: Candidate 15033.1 from Observation 59168.67. This candidate has a DM of 144.42 cm^{-3} pc, a pulse width of 1.05 ms, a flux density of 7.24 Jy, and a S/N of 6.38. In the top panel, there is a clear peak in flux. The middle panel shows a vertical line in dedispersed frequency, as expected. The bottom panel shows a clear peak in DM, ruling out most forms of RFI.

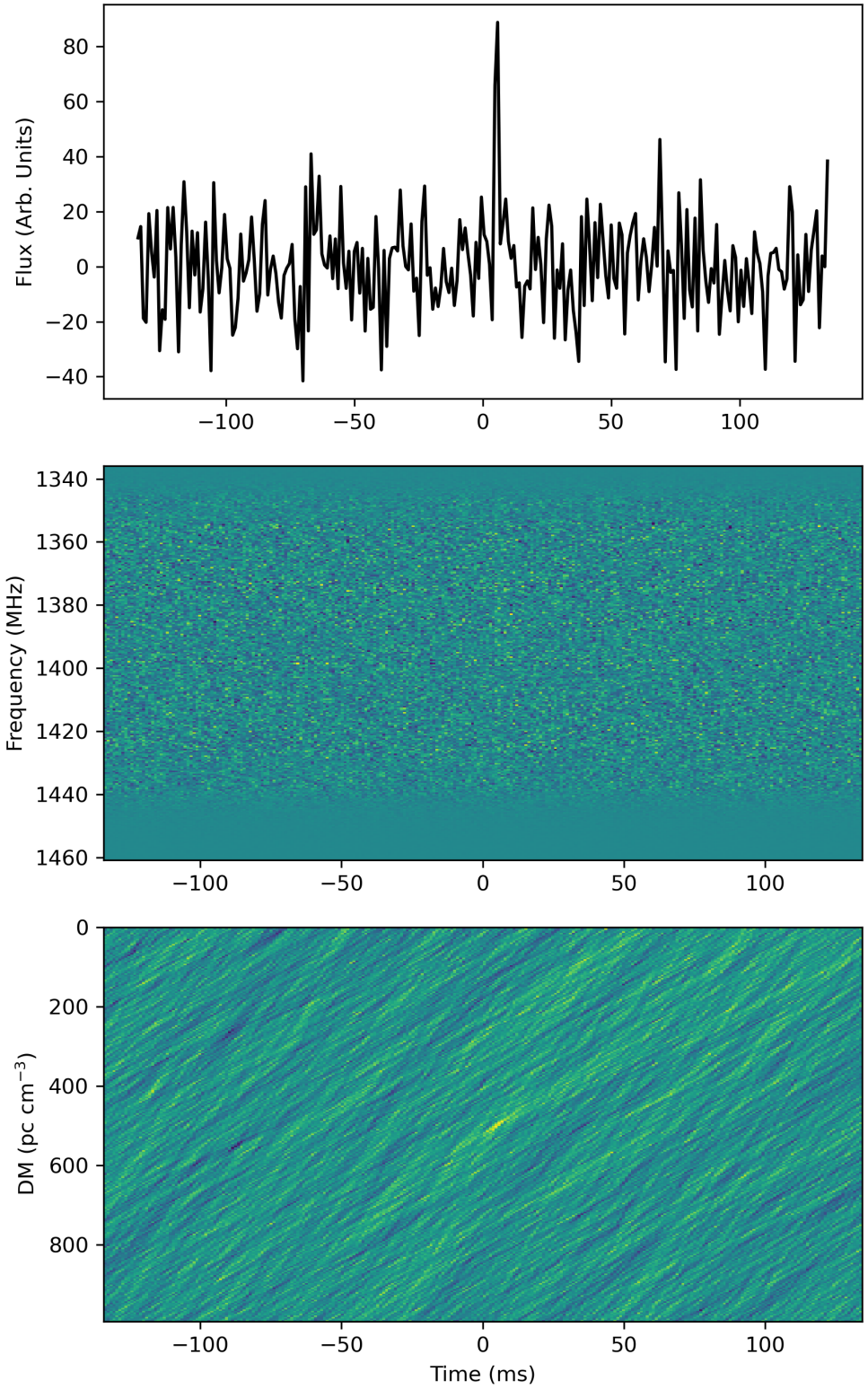

FIGURE 4.4: Candidate 6537.1 from Observation 59330.54. This candidate has a DM of 496.83 cm^{-3} pc, a pulse width of 2.1 ms, a flux density of 5.95 Jy, and a S/N of 7.41. In the top panel, there is a clear peak in flux. The middle panel shows a faint vertical line in dedispersed frequency. The bottom panel shows a slightly larger peak in DM, but still consistent with an astrophysical source.

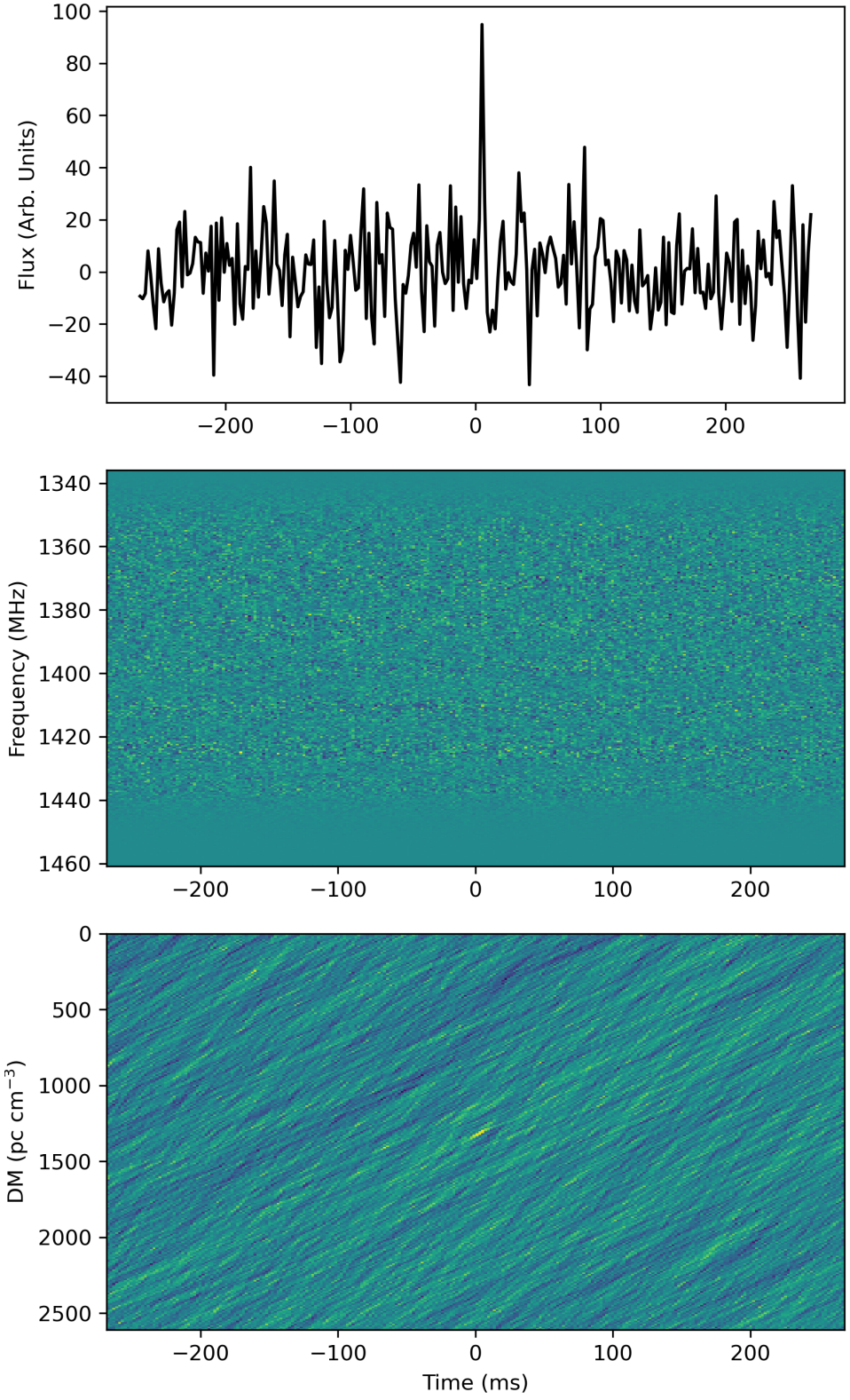

FIGURE 4.5: Candidate 2560.0 from Observation 59496.39. This candidate has a DM of 1305.33 cm^{-3} pc, a pulse width of 4.19 ms, a flux density of 3.8 Jy, and a S/N of 6.7. The top panel shows a clear peak in flux. Both the middle and bottom panels have faint features, but there is a vertical line in dedispersed frequency as well as a peak in DM.

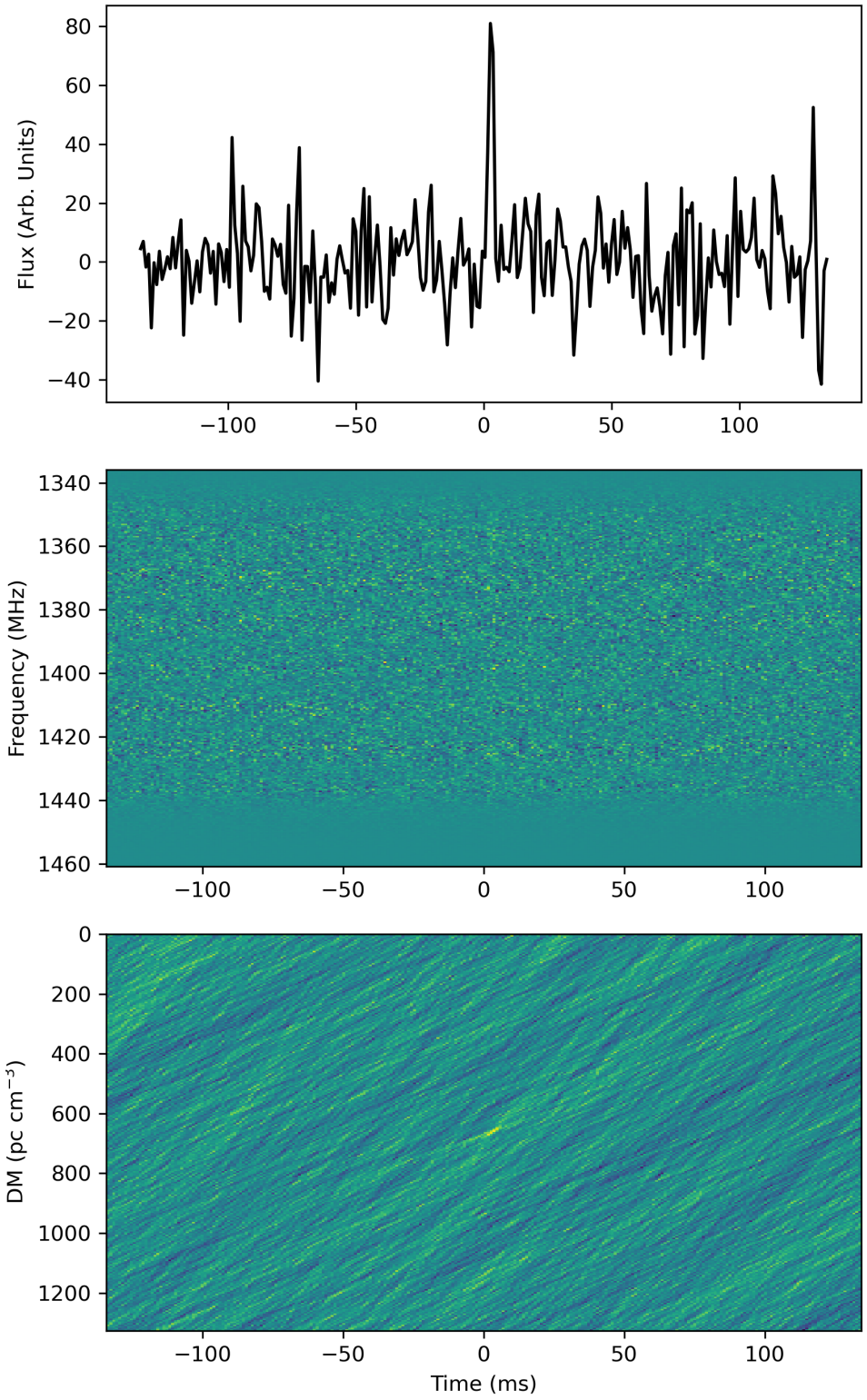

FIGURE 4.6: Candidate 7801.27 from Observation 59536.52. This candidate has a DM of 663.37 cm^{-3} pc, a pulse width of 2.1 ms, a flux density of 5.32 Jy, and a S/N of 6.63. Again, there is a clear peak in flux with a faint line in frequency and faint peak in DM.

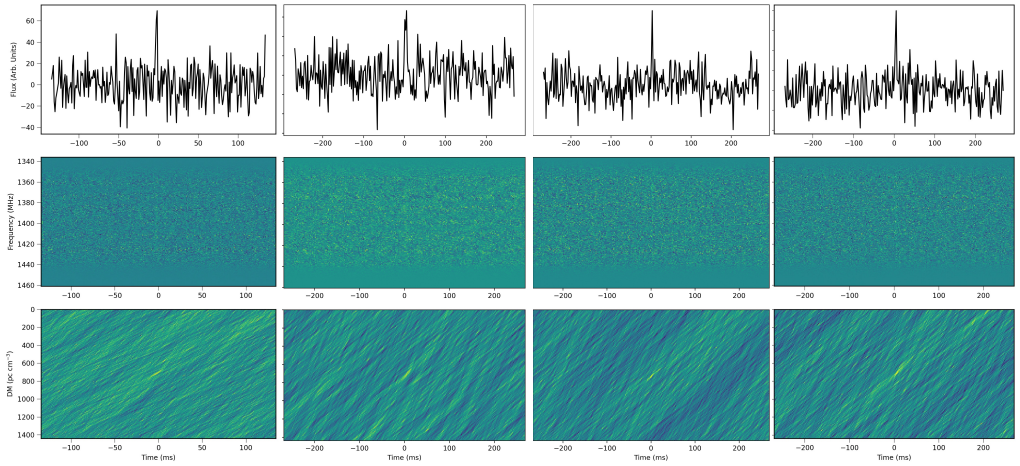

FIGURE 4.7: The four bursts with a DM of 719.052 cm^{-3} pc. While they are less clear than the individual bursts in earlier figures, the repeated DM gives them greater significance.

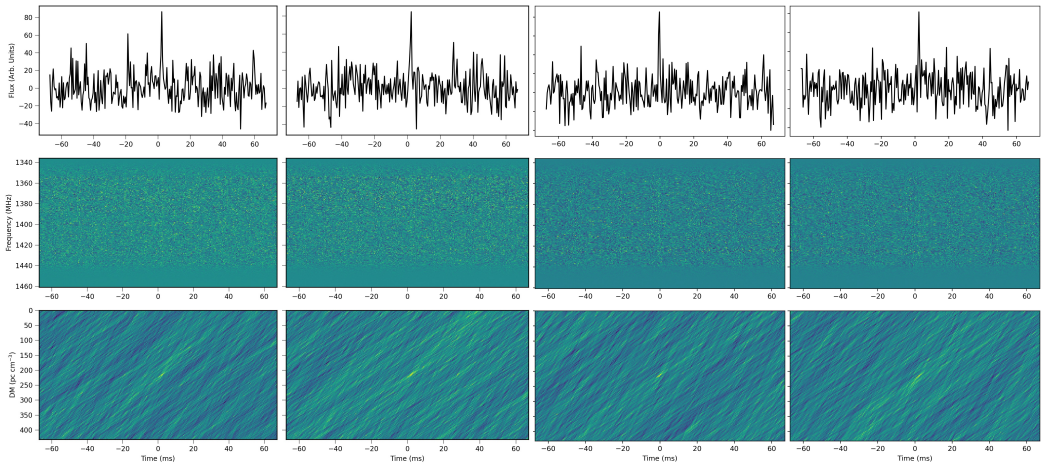

FIGURE 4.8: The four bursts with a DM of 215.746 cm^{-3} pc. These bursts are more prominent than those with DM=719.052 cm^{-3} pc.

CHAPTER 5: Conclusion

An FRB-like burst was detected from a Galactic magnetar in 2020 (Bochenek et al. 2020; CHIME/FRB Collaboration et al. 2020), allowing researchers to constrain a Galactic magnetar burst rate. We observed Messier 82, hoping to detect a Fast Radio Burst (FRB) and strengthen the growing connection between FRBs and magnetars. We then assumed that magnetar burst rate scales with star formation rate. Since M82's star formation rate is 40 times greater than the Milky Way's, we expected to detect an FRB within the first 25 days of observation.

Using the 20 meter telescope at the Green Bank Observatory, we observed M82 for 28.2 days, more than enough time to reach a detection if our hypothesis holds. In those 28.2 days, we found 291 candidate bursts, of which the 27 best have been listed in Table 4.1 and included in Appendix B. None of those bursts have a signal-to-noise ratio greater than 10, which is required for a burst to be entered into an FRB catalog.

It is possible, and perhaps likely that the bursts we did detect are statistical flukes. There is a chance that incoherent signals in dispersed data can be dedispersed into a configuration that seems to represent a source. These pulses may be no more than low-level noise combined to mimic an astrophysical burst. However, it is also possible that these are astrophysical bursts that a telescope with a lower noise level would be able to detect more clearly.

We also did not detect a repeating FRB. We found two DM trials with four bursts each, resulting in a confidence level of 99.6%. The gold standard for scientific detections is 5σ, or 99.99995%. Thus, our repeating bursts are not classified as FRBs.

The lack of detection at this stage leads us to conclude that further observation of M82 with the 20 meter telescope would produce diminishing returns. While a detection is still possible, it may be more worthwhile to pivot to another telescope. The telescope has likely reached its sensitivity limit, meaning that either bursts from M82 are not bright enough to sufficiently outweigh the noise or bursts are rarer than expected. If a burst with the inherent luminosity of the Galactic burst

were to take place in M82, the 20 meter telescope would be able to detect it. If FRBs are taking place in M82, they must be at lower luminosity levels than previously supposed.

Since we do not have a definitive detection, our initial assumption may not be valid. If we were to preserve the proposed relationship between magnetar burst rate and star formation rate, M82's star formation rate must be less than 3.6 times that of the Milky Way, a clear contradiction of previous results.

The numerical mismatch between our results and the literature values fully disproves the initial assumption: magnetar burst rate cannot scale with star formation rate. M82 either does not have the predicted overdensity of magnetars or those magnetars are remarkably quiescent.

The magnetar burst rate from M82 remains unknown, though it is much lower than previously anticipated. While it is probable that magnetars within M82 release energy in bursts, the rate of these bursts is quite low. Or, rather, the rate of magnetar bursts with detectable brightnesses is lower than one burst in 28.2 days.

The lack of FRBs from M82 may also indicate that not all FRBs have magnetar origins. While magnetars certainly contribute at least part of the FRB population, it is possible that the bursts arise from different sources. Knowledge of FRB origins will certainly take more time and many more studies before any definitive answers are found.

5.1 Future Work

The future of FRB research is wide and bright. There are countless projects planned, and many are currently running. In the realm of M82, continued searching with the 20 meter telescope at GBO is not useful. The 20 meter telescope is limited by its low sensitivity due to the smaller collecting area.

The more promising route is an instrument called ALPACA, or the Advanced Cryogenic L-band Phased Array Camera for Arecibo. ALPACA is being devloped by Brian Jeffs at Brigham Young University and has received a National Science

Foundation grant[1]. Since the tragic decomissioning of Arecibo in 2020, researchers have been lobbying for ALPACA to be installed at the Robert C. Byrd Green Bank Telescope (GBT). The instrument has not yet been completed, but it will hopefully be brought to the GBT soon.

With ALPACA, the GBT could image the entirety of M82 at once. Currently, M82 is larger than the beam size of the GBT, meaning that the telescope cannot simultaneously observe the entire galaxy. Burst rates cannot be determined without simultaneous coverage of the entire source, meaning that the GBT could not previously monitor M82. With the addition of ALPACA, the GBT could replace the 20 meter telescope to observe M82. The GBT has a larger collecting area and greater sensitivity, meaning that it will be able to detect dimmer bursts with higher S/Ns than the 20 meter telescope. These observations will also likely be able to constrain the magnetar population of M82.

[1]https://nsf.gov/awardsearch/showAward?AWD_ID=1636645

APPENDIX A: Observation List

In Table A.1, we list all of the observation sessions for this project. All observations were made with the 20 meter telescope at Green Bank Observatory. The first column in the table gives the date of the observation. The second column gives the Modified Julian Date (MJD) of the observation. The final column gives the duration of the observing session in hours. Our target duration for an observing session was 10 hours.

Date	MJD	Duration (hr)
2020/10/13	59135.8	2.0
2020/10/14	59136.3	10.0
2020/10/16	59138.2	8.0
2020/10/18	59240.4	6.0
2020/10/19	59140.3	6.0
2020/10/20	59142.6	6.0
2020/10/22	59144.1	10.0
2020/10/24	59146.0	5.6
2020/10/14	59146.2	12.0
2020/10/15	59147.0	12.0
2020/10/26	59148.2	12.0
2020/10/27	59149.5	6.0
2020/10/28	59150.6	6.0
2020/11/02	59155.6	10.0
2020/11/03	59156.2	10.0
2020/11/04	59157.1	10.0
2020/11/05	59158.2	10.0
2020/11/12	59165.1	10.0
2020/11/12	59165.5	10.0
2020/11/13	59166.1	10.0
2020/11/13	59166.8	2.0
2020/11/15	59168.7	7.9
2020/11/16	59169.6	4.0

Continued on next page

Table A.1 – continued from previous page

Date	MJD	Duration (hr)
2020/11/17	59170.1	10.0
2020/11/20	59173.8	5.4
2020/11/21	59174.0	0.6
2020/11/22	59175.6	8.7
2020/11/23	59176.0	8.6
2020/11/23	59176.6	5.4
2020/11/24	59177.2	0.2
2020/11/25	59178.1	5.4
2020/11/27	59180.7	6.4
2020/11/29	59182.1	4.9
2020/12/01	59184.2	10.0
2020/12/02	59185.6	8.5
2020/12/07	59190.9	3.3
2020/12/08	59191.6	1.4
2020/12/09	59192.5	10.0
2020/12/10	59193.2	10.0
2020/12/18	59201.9	2.8
2020/12/19	59202.0	10.0
2020/12/20	59203.6	7.5
2020/12/23	59206.2	0.6
2020/12/23	59206.6	9.0
2020/12/24	59207.8	2.7
2020/12/26	59209.5	10.0
2021/01/19	59233.1	10.0
2021/01/19	59233.9	2.2
2021/01/20	59234.8	4.5
2021/01/21	59235.0	10.0
2021/01/22	59236.6	4.8
2021/01/22	59236.8	1.2
2021/01/22	59238.9	3.3
2021/01/23	59237.0	0.8

Continued on next page

Table A.1 – continued from previous page

Date	MJD	Duration (hr)
2021/01/25	59239.8	4.0
2021/01/16	59240.7	4.0
2021/01/28	59242.1	4.5
2021/03/31	59304.8	8.0
2021/01/20	59234.8	4.5
2021/01/21	59235.0	10.0
2021/01/22	59236.6	4.8
2021/01/22	59236.8	1.2
2021/01/22	59236.9	3.3
2021/01/23	59237.0	0.8
2021/01/25	59239.8	4.0
2021/01/26	59240.7	4.0
2021/01/28	59242.1	4.5
2021/02/05	59250.8	0.7
2021/02/08	59253.9	6.0
2021/03/31	59304.8	8.0
2021/04/03	59307.8	10.0
2021/04/26	59330.5	0.0
2021/04/26	59330.5	10.0
2021/07/08	59403.8	10.0
2021/09/28	59485.6	3.8
2021/09/28	59485.6	4.4
2021/09/28	59485.9	0.4
2021/09/29	59486.0	0.1
2021/09/29	59486.0	0.7
2021/09/29	59486.0	3.8
2021/09/29	59486.2	0.0
2021/09/30	59487.8	4.2
2021/10/01	59488.1	10.0
2021/10/01	59488.7	6.5
2021/10/02	59489.0	10.0

Continued on next page

Table A.1 – continued from previous page

Date	MJD	Duration (hr)
2021/10/05	59492.1	10.0
2021/10/08	59495.7	0.4
2021/10/08	59495.7	6.7
2021/10/09	59496.4	4.7
2021/10/09	59496.7	7.8
2021/10/10	59497.1	1.7
2021/10/10	59497.2	10.0
2021/10/19	59506.8	4.3
2021/10/20	59507.0	10.0
2021/10/26	59513.5	10.0
2021/10/27	59514.6	9.2
2021/10/28	59515.2	7.6
2021/10/29	59516.2	10.0
2021/11/03	59521.6	9.3
2021/11/04	59522.3	5.8
2021/11/04	59522.6	9.1
2021/11/05	59523.3	7.9
2021/11/05	59523.6	8.4
2021/11/06	59524.0	10.0
2021/11/11	59529.2	10.0
2021/11/18	59536.5	10.0
2021/11/19	59537.6	10.0
2021/11/20	59538.1	10.0
2021/12/02	59550.5	10.0
2022/01/21	59600.6	8.6
2022/01/22	59601.7	1.9

TABLE A.1: Dates and lengths of observations on the 20m telescope

APPENDIX B: Best FRB Figures

In this appendix, we show the FETCH outputs for all 27 of the 'best' candidates, complete with their meta data on the side. The three panels are explained in Section 3.3 of the text. The meta data is explained here. The first entry is the 'basename', or the project name. Next, 'bw' represents the total bandwidth, in MHz. This should be the same for every candidate. 'cand_id' is the full candidate name, consisting of the time at the beginning of the observation, the time at which the candidate was found, the dispersion measure, and the S/N. The 'center_freq' gives the center frequency of the bandwidth, consistent across every candidate. 'dec_deg' gives the declination of the telescope in degrees. This should be fairly consistent across candidates since all sources come from M82. 'dm' gives the candiate's DM. 'dm_opt' is an optimization flag that is not used in this analysis. 'dtype' is an internal code used for communicating between modules in the software package. 'fch1' gives the frequency of the first channel of the observation, which should be consistent. 'filename' is the name of the output file. 'filepath' gives the file's output location. 'foff' refers to the channel bandwidth relative to the highest frequency channel, hence the negative sign. 'format' gives the format of the output file, a 'fil'. 'frequency_discrimination_factor', 'gb', and 'gf are internal flags used by FETCH. 'label' gives FETCH's designation of the candiate. A label of 1 means that the candidate is considered an astrophysical source. 'native_foff' is the original channel bandwidth. All native values should be equal to the values used by HEIMDALL and FETCH. 'native_nchans' is the number of channels from the telescope itself. 'native_nspectra' is the number of spectra from the telescope. 'native_tsamp' is the sampling time of the telescope. 'nbits' is the number of bits used to quantize the analog signal. 'nchans' is the number of channels used. 'npol' is the number of polarization channels. We are only considering total intensity, giving a value of 1. 'nspectra' is the number of spectra used. 'ra_deg' is the right ascension in degrees. This should be fairly consistent, since all candidates are in M82. 'snr' is the signal-to-noise ratio. 'snr_opt' is an optimization flag that is not used in this analysis. 'source_name' is the source's name, M82 for all candidates. 'tcand' gives the time elapsed from the beginning of an observation when a pulse was found. 'time_decimation_factor' is the number of adjacent time samples that

have been added together. 'tsamp' is the sampling time of the telescope, consistent for all candidates. 'tstart' gives the MJD of the beginning of the observation. 'tstart_utc' gives the time of the start of the observation in UTC. 'width' gives the width of the pulse in time bins. Each bin is the sampling time.

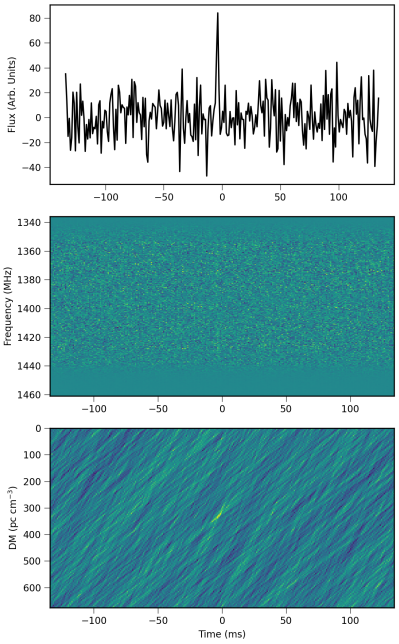

basename : Skynet_59135_M82_46921_56403_0001
bw : -125.0
cand_id : cand_tstart_59135.773055555554_tcand_610.7930000_dm_337.55500_snr_6.13170
center_freq : 1398.388671875
dec_deg : 69.68001666666669
dm : 337.555
dm_opt : -1
dtype : uint16
fch1 : 1460.888671875
filename : Skynet_59135_M82_46921_56403_0001.fil
filepath : /notebook/scratch/20m
foff : -0.48828125
format : fil
frequency_decimation_factor : 1
gb : 40.591514533038755
gl : -38.61429976871386
label : 1
native_foff : -0.48828125
native_nchans : 256
native_nspectra : 54950816.0
native_tsamp : 0.000131072
nbits : 16
nchans : 256
npol : 1
nspectra : 54950816
ra_deg : 149.05620833333336
snr : 6.1317
snr_opt : -1
source_name : M82
tcand : 610.793
time_decimation_factor : 1
tsamp : 0.000131072
tstart : 59135.77305555555
tstart_utc : 2020-10-13T18:33:12.000
width : 16

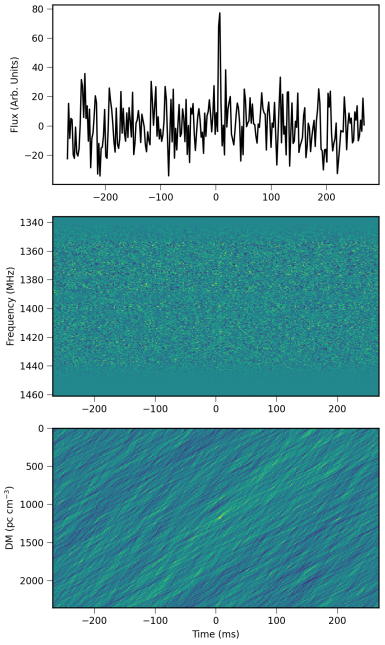

basename : Skynet_59140_M82_47141_56704_0001
bw : -125.0
cand_id : cand_tstart_59140.262812499997_tcand_4890.5000000_dm_1177.59000_snr_6.43628
center_freq : 1398.388671875
dec_deg : 69.68136666666668
dm : 1177.59
dm_opt : -1
dtype : uint16
fch1 : 1460.888671875
filename : Skynet_59140_M82_47141_56704_0001.fil
filepath : /notebook/scratch/M82/59140
foff : -0.48828125
format : fil
frequency_decimation_factor : 1
gb : 40.56401690046356
gl : -38.59044576077952
label : 1
native_foff : -0.48828125
native_nchans : 256
native_nspectra : 164866112.0
native_tsamp : 0.000131072
nbits : 16
nchans : 256
npol : 1
nspectra : 164866112
ra_deg : 148.96145833333333
snr : 6.43628
snr_opt : -1
source_name : M82
tcand : 4890.5
time_decimation_factor : 1
tsamp : 0.000131072
tstart : 59140.2628125
tstart_utc : 2020-10-18T06:18:27.000
width : 32

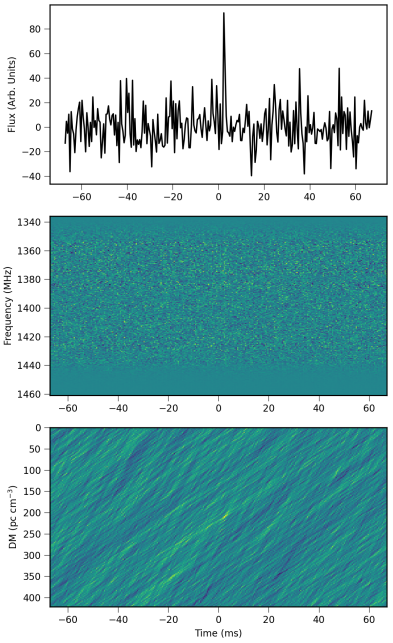

basename : Skynet_59150_M82_48633_57875_0001
bw : -125.0
cand_id : cand_tstart_59150.631956018522_tcand_7532.2200000_dm_210.43300_snr_6.11991
center_freq : 1398.388671875
dec_deg : 69.68034444444444
dm : 210.433
dm_opt : -1
dtype : uint16
fch1 : 1460.888671875
filename : Skynet_59150_M82_48633_57875_0001.fil
filepath : /notebook/scratch/M82/59150
foff : -0.48828125
format : fil
frequency_decimation_factor : 1
gb : 40.55858263826767
gl : -38.58365614317697
label : 1
native_foff : -0.48828125
native_nchans : 256
native_nspectra : 164855904.0
native_tsamp : 0.000131072
nbits : 16
nchans : 256
npol : 1
nspectra : 164855904
ra_deg : 148.94008333333332
snr : 6.11991
snr_opt : -1
source_name : M82
tcand : 7532.22
time_decimation_factor : 1
tsamp : 0.000131072
tstart : 59150.63195601852
tstart_utc : 2020-10-28T15:10:01.000
width : 8

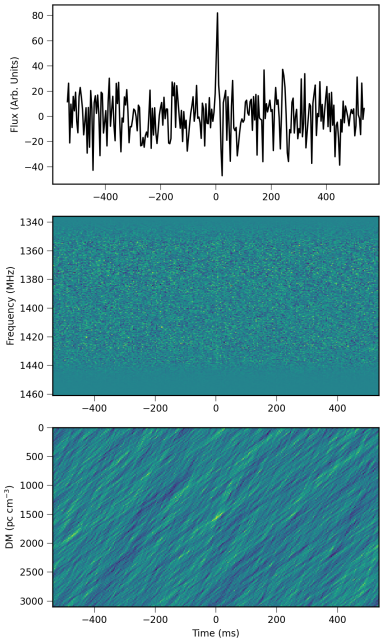

basename : Skynet_59168_M82_50868_60359_0001
bw : -125.0
cand_id : cand_tstart_59168.672743055555_tcand_7341.7200000_dm_1549.58000_snr_6.26709
center_freq : 1398.388671875
dec_deg : 69.67916944444445
dm : 1549.58
dm_opt : -1
dtype : uint16
fch1 : 1460.888671875
filename : Skynet_59168_M82_50868_60359_0001.fil
filepath : /notebook/scratch/M82/59168
foff : -0.48828125
format : fil
frequency_decimation_factor : 1
gb : 40.56362917229805
gl : -38.58651898567308
label : 1
native_foff : -0.48828125
native_nchans : 256
native_nspectra : 215752192.0
native_tsamp : 0.000131072
nbits : 16
nchans : 256
npol : 1
nspectra : 215752192
ra_deg : 148.9555416666667
snr : 6.2670900000000005
snr_opt : -1
source_name : M82
tcand : 7341.72
time_decimation_factor : 1
tsamp : 0.000131072
tstart : 59168.672743055555
tstart_utc : 2020-11-15T16:08:45.000
width : 64

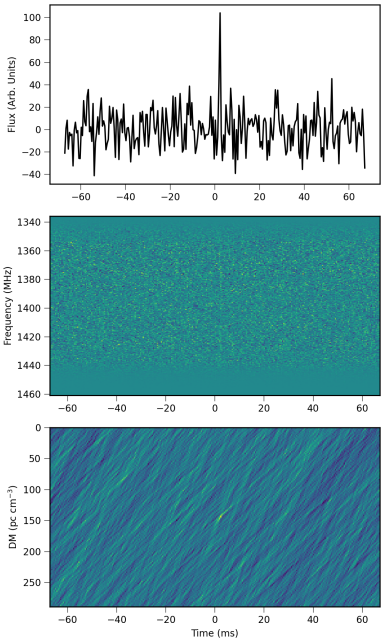

basename : Skynet_59168_M82_50868_60359_0001
bw : -125.0
cand_id : cand_tstart_59168.672743055555_tcand_15033.1000000_dm_144.42000_snr_6.37629
center_freq : 1398.388671875
dec_deg : 69.67916944444445
dm : 144.42
dm_opt : -1
dtype : uint16
fch1 : 1460.888671875
filename : Skynet_59168_M82_50868_60359_0001.fil
filepath : /notebook/scratch/M82/59168
foff : -0.48828125
format : fil
frequency_decimation_factor : 1
gb : 40.56362917229805
gl : -38.58651898567308
label : 1
native_foff : -0.48828125
native_nchans : 256
native_nspectra : 215752192.0
native_tsamp : 0.000131072
nbits : 16
nchans : 256
npol : 1
nspectra : 215752192
ra_deg : 148.9555416666667
snr : 6.37629
snr_opt : -1
source_name : M82
tcand : 15033.1
time_decimation_factor : 1
tsamp : 0.000131072
tstart : 59168.672743055555
tstart_utc : 2020-11-15T16:08:45.000
width : 8

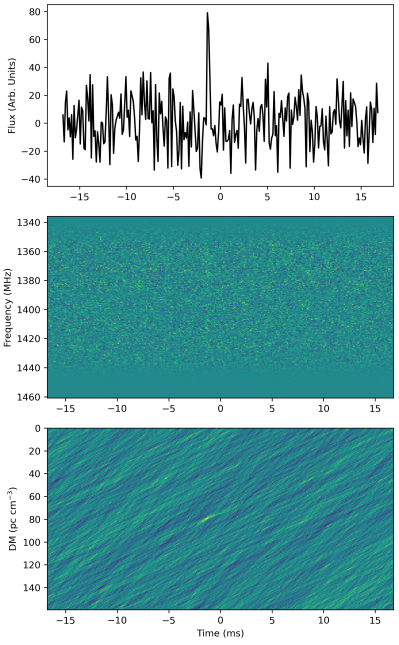

basename : Skynet_59176_M82_51036_60544_0001
bw : -125.0
cand_id : cand_tstart_59176.026562500003_tcand_5923.8900000_dm_79.73780_snr_6.91024
center_freq : 1398.388671875
dec_deg : 69.67896666666668
dm : 79.7378
dm_opt : -1
dtype : uint16
fch1 : 1460.888671875
filename : Skynet_59176_M82_51036_60544_0001.fil
filepath : /notebook/scratch/59176
foff : -0.48828125
format : fil
frequency_decimation_factor : 1
gb : 40.58145500687454
gl : -38.60305629261555
label : 1
native_foff : -0.48828125
native_nchans : 256
native_nspectra : 236599200.0
native_tsamp : 0.000131072
nbits : 16
nchans : 256
npol : 1
nspectra : 236599200
ra_deg : 149.0183333333333
snr : 6.910239999999999
snr_opt : -1
source_name : M82
tcand : 5923.89
time_decimation_factor : 1
tsamp : 0.000131072
tstart : 59176.0265625
tstart_utc : 2020-11-23T00:38:15.000
width : 2

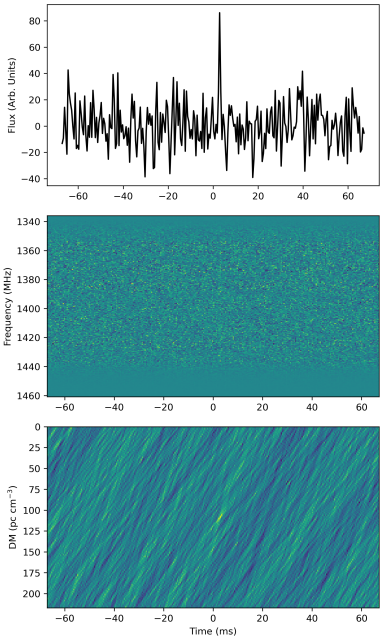

basename : Skynet_59176_M82_51036_60544_0001
bw : -125.0
cand_id : cand_tstart_59176.026562500003_tcand_16090.2000000_dm_108.54600_snr_6.19286
center_freq : 1398.388671875
dec_deg : 69.67896666666668
dm : 108.546
dm_opt : -1
dtype : uint16
fch1 : 1460.888671875
filename : Skynet_59176_M82_51036_60544_0001.fil
filepath : /notebook/scratch/59176
foff : -0.48828125
format : fil
frequency_decimation_factor : 1
gb : 40.58145500687454
gl : -38.60305629261555
label : 1
native_foff : -0.48828125
native_nchans : 256
native_nspectra : 236599200.0
native_tsamp : 0.000131072
nbits : 16
nchans : 256
npol : 1
nspectra : 236599200
ra_deg : 149.0183333333333
snr : 6.19286
snr_opt : -1
source_name : M82
tcand : 16090.2
time_decimation_factor : 1
tsamp : 0.000131072
tstart : 59176.0265625
tstart_utc : 2020-11-23T00:38:15.000
width : 8

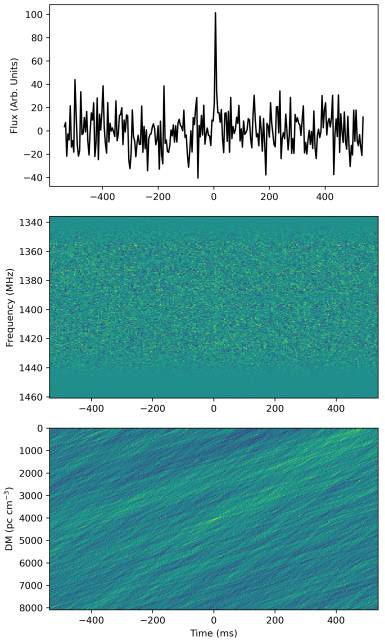

basename : Skynet_59184_M82_51212_143_0001
bw : -125.0
cand_id : cand_tstart_59184.207789351851_tcand_7337.4300000_dm_4044.03000_snr_6.50148
center_freq : 1398.388671875
dec_deg : 69.68243611111112
dm : 4044.03
dm_opt : -1
dtype : uint16
fch1 : 1460.888671875
filename : Skynet_59184_M82_51212_143_0001.fil
filepath : /notebook/scratch/M82/59184
foff : -0.48828125
format : fil
frequency_decimation_factor : 1
gb : 40.56613122990349
gl : -38.5941776614153
label : 1
native_foff : -0.48828125
native_nchans : 256
native_nspectra : 274780000.0
native_tsamp : 0.000131072
nbits : 16
nchans : 256
npol : 1
nspectra : 274780000
ra_deg : 148.97116666666665
snr : 6.50148
snr_opt : -1
source_name : M82
tcand : 7337.43
time_decimation_factor : 1
tsamp : 0.000131072
tstart : 59184.20778935185
tstart_utc : 2020-12-01T04:59:13.000
width : 64

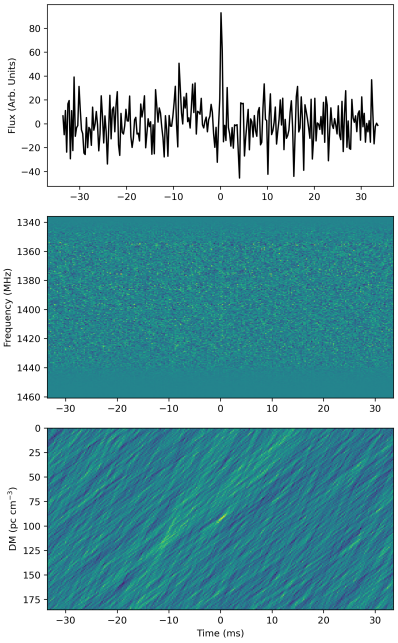

basename : Skynet_59192_M82_51513_485_0001
bw : -125.0
cand_id : cand_tstart_59192.477164351854_tcand_4819.4000000_dm_92.83800_snr_6.31344
center_freq : 1398.388671875
dec_deg : 69.68051944444444
dm : 92.838
dm_opt : -1
dtype : uint16
fch1 : 1460.888671875
filename : Skynet_59192_M82_51513_485_0001.fil
filepath : /notebook/scratch/M82/59192
foff : -0.48828125
format : fil
frequency_decimation_factor : 1
gb : 40.564898874192934
gl : -38.5899064077704
label : 1
native_foff : -0.48828125
native_nchans : 256
native_nspectra : 274779712.0
native_tsamp : 0.000131072
nbits : 16
nchans : 256
npol : 1
nspectra : 274779712
ra_deg : 148.96283333333335
snr : 6.31344
snr_opt : -1
source_name : M82
tcand : 4819.4
time_decimation_factor : 1
tsamp : 0.000131072
tstart : 59192.477164351854
tstart_utc : 2020-12-09T11:27:07.000
width : 4

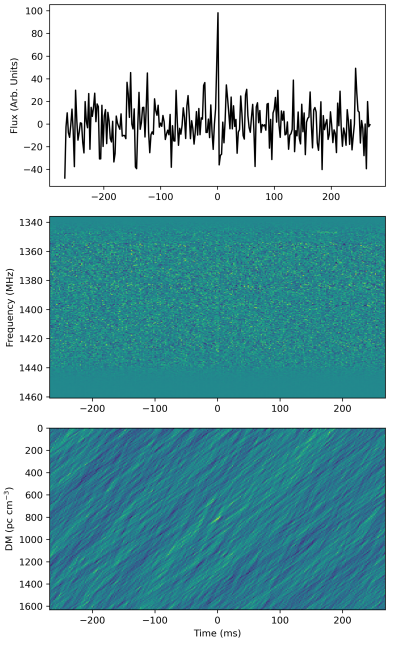

basename : Skynet_59234_M82_51783_749_0001
bw : -125.0
cand_id : cand_tstart_59235.026782407411_tcand_5662.2800000_dm_815.97800_snr_6.47749
center_freq : 1398.388671875
dec_deg : 69.67904722222221
dm : 815.9780000000002
dm_opt : -1
dtype : uint16
fch1 : 1460.888671875
filename : Skynet_59234_M82_51783_749_0001.fil
filepath : /notebook/scratch/M82/59234b
foff : -0.48828125
format : fil
frequency_decimation_factor : 1
gb : 40.56801418262152
gl : -38.590465389079355
label : 1
native_foff : -0.48828125
native_nchans : 256
native_nspectra : 274771872.0
native_tsamp : 0.000131072
nbits : 16
nchans : 256
npol : 1
nspectra : 274771872
ra_deg : 148.97083333333336
snr : 6.47749
snr_opt : -1
source_name : M82
tcand : 5662.28
time_decimation_factor : 1
tsamp : 0.000131072
tstart : 59235.02678240741
tstart_utc : 2021-01-21T00:38:34.000
width : 32

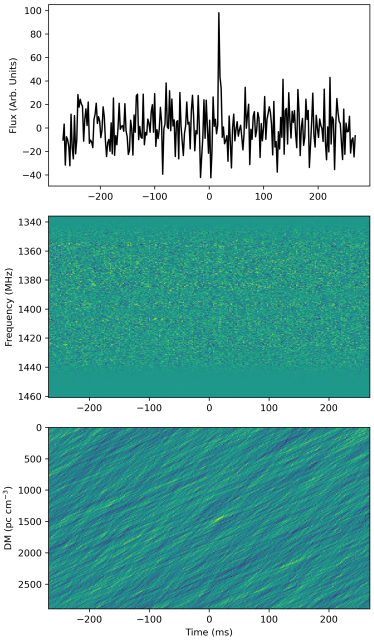

basename : Skynet_59240_M82_51834_810_0001
bw : -125.0
cand_id : cand_tstart_59240.666956018518_tcand_12461.7000000_dm_1446.85000_snr_6.87833
center_freq : 1398.388671875
dec_deg : 69.67907777777779
dm : 1446.85
dm_opt : -1
dtype : uint16
fch1 : 1460.888671875
filename : Skynet_59240_M82_51834_810_0001.fil
filepath : /notebook/scratch/M82/59240
foff : -0.48828125
format : fil
frequency_decimation_factor : 1
gb : 40.56551636697671
gl : -38.588153766558946
label : 1
native_foff : -0.48828125
native_nchans : 256
native_nspectra : 109910368.0
native_tsamp : 0.000131072
nbits : 16
nchans : 256
npol : 1
nspectra : 109910368
ra_deg : 148.96204166666666
snr : 6.87833
snr_opt : -1
source_name : M82
tcand : 12461.7
time_decimation_factor : 1
tsamp : 0.000131072
tstart : 59240.66695601852
tstart_utc : 2021-01-26T16:00:25.000
width : 32

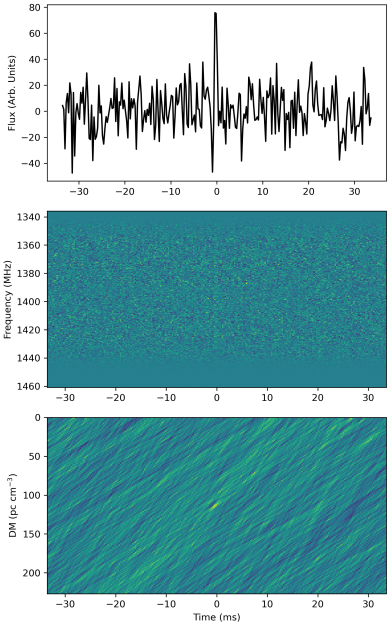

basename : Skynet_59307_M82_53371_2333_0001
bw : -125.0
cand_id : cand_tstart_59307.814166666663_tcand_1225.4600000_dm_113.52300_snr_6.05512
center_freq : 1398.388671875
dec_deg : 69.68007777777778
dm : 113.523
dm_opt : -1
dtype : uint16
fch1 : 1460.888671875
filename : Skynet_59307_M82_53371_2333_0001.fil
filepath : /notebook/scratch/M82/59307
foff : -0.48828125
format : fil
frequency_decimation_factor : 1
gb : 40.62932211634208
gl : -38.65039264339961
label : 1
native_foff : -0.48828125
native_nchans : 256
native_nspectra : 274828448.0
native_tsamp : 0.000131072
nbits : 16
nchans : 256
npol : 1
nspectra : 274828448
poln_order : I
ra_deg : 149.19066666666663
snr : 6.05512
snr_opt : -1
source_name : M82
tcand : 1225.46
time_decimation_factor : 1
tsamp : 0.000131072
tstart : 59307.81416666666
tstart_utc : 2021-04-03T19:32:24.000
width : 4

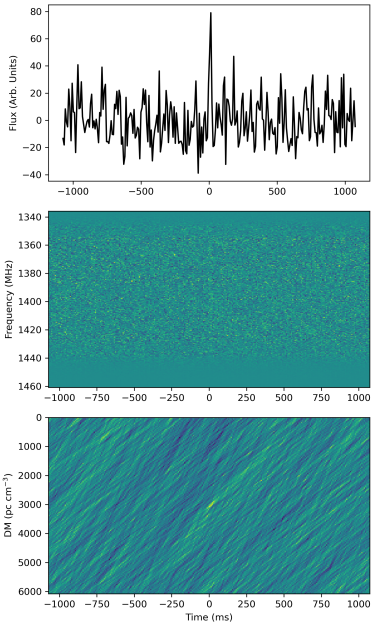

basename : Skynet_59307_M82_53371_2333_0001
bw : -125.0
cand_id : cand_tstart_59307.814166666663_tcand_29817.5000000_dm_3040.06000_snr_6.62144
center_freq : 1398.388671875
dec_deg : 69.68007777777778
dm : 3040.06
dm_opt : -1
dtype : uint16
fch1 : 1460.888671875
filename : Skynet_59307_M82_53371_2333_0001.fil
filepath : /notebook/scratch/M82/59307
foff : -0.48828125
format : fil
frequency_decimation_factor : 1
gb : 40.62932211634208
gl : -38.65039264339961
label : 1
native_foff : -0.48828125
native_nchans : 256
native_nspectra : 274828448.0
native_tsamp : 0.000131072
nbits : 16
nchans : 256
npol : 1
nspectra : 274828448
poln_order : I
ra_deg : 149.19066666666663
snr : 6.62144
snr_opt : -1
source_name : M82
tcand : 29817.5
time_decimation_factor : 1
tsamp : 0.000131072
tstart : 59307.81416666666
tstart_utc : 2021-04-03T19:32:24.000
width : 128

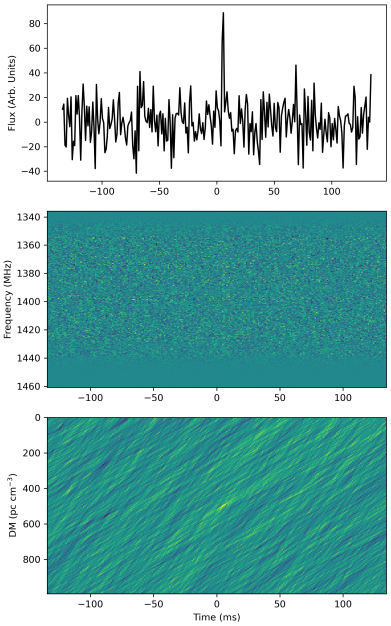

basename : Skynet_59330_M82_59121_8005_0001
bw : -125.0
cand_id : cand_tstart_59330.543611111112_tcand_6537.1000000_dm_496.82500_snr_7.40996
center_freq : 1398.388671875
dec_deg : 69.67995833333333
dm : 496.825
dm_opt : -1
dtype : uint16
fch1 : 1460.888671875
filename : Skynet_59330_M82_59121_8005_0001.fil
filepath : /notebook/scratch/M82/59330b
foff : -0.48828125
format : fil
frequency_decimation_factor : 1
gb : 40.61930210226126
gl : -38.640637873111785
label : 1
native_foff : -0.48828125
native_nchans : 256
native_nspectra : 274766016.0
native_tsamp : 0.000131072
nbits : 16
nchans : 256
npol : 1
nspectra : 274766016
poln_order : I
ra_deg : 149.15479166666665
snr : 7.409960000000001
snr_opt : -1
source_name : M82
tcand : 6537.1
time_decimation_factor : 1
tsamp : 0.000131072
tstart : 59330.54361111111
tstart_utc : 2021-04-26T13:02:48.000
width : 16

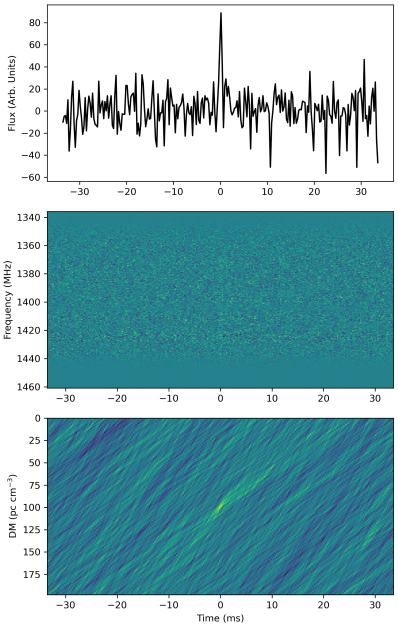

basename : Skynet_59485_M82_62247_11074_0456
bw : -125.0
cand_id : cand_tstart_59485.581840277780_tcand_7068.6100000_dm_98.96520_snr_6.32709
center_freq : 1398.388671875
dec_deg : 69.67973611111113
dm : 98.9652
dm_opt : -1
dtype : uint16
fch1 : 1460.888671875
filename : Skynet_59485_M82_62247_11074_0456.fil
filepath : /notebook/scratch/M82/59485b
foff : -0.48828125
format : fil
frequency_decimation_factor : 1
gb : 40.591044692256006
gl : -38.613398438173874
label : 1
native_foff : -0.48828125
native_nchans : 256
native_nspectra : 120037408.0
native_tsamp : 0.000131072
nbits : 16
nchans : 256
npol : 1
nspectra : 120037408
poln_order : I
ra_deg : 149.05395833333333
snr : 6.32709
snr_opt : -1
source_name : M82
tcand : 7068.61
time_decimation_factor : 1
tsamp : 0.000131072
tstart : 59485.58184027778
tstart_utc : 2021-09-28T13:57:51.000
width : 4

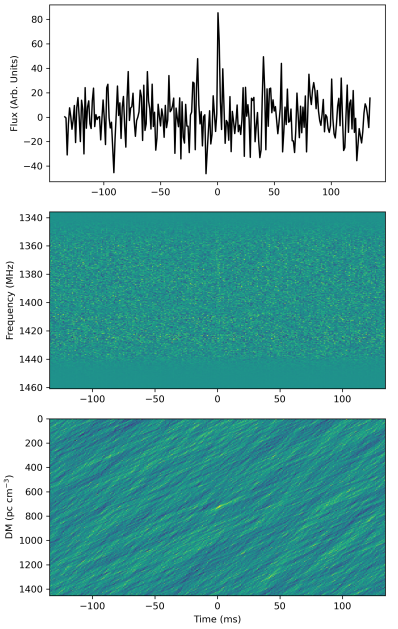

basename : Skynet_59485_M82_62247_11074_0456
bw : -125.0
cand_id : cand_tstart_59485.581840277780_tcand_8230.1600000_dm_727.37300_snr_6.76316
center_freq : 1398.388671875
dec_deg : 69.67973611111113
dm : 727.373
dm_opt : -1
dtype : uint16
fch1 : 1460.888671875
filename : Skynet_59485_M82_62247_11074_0456.fil
filepath : /notebook/scratch/M82/59485b
foff : -0.48828125
format : fil
frequency_decimation_factor : 1
gb : 40.591044692256006
gl : -38.613398438173874
label : 1
native_foff : -0.48828125
native_nchans : 256
native_nspectra : 120037408.0
native_tsamp : 0.000131072
nbits : 16
nchans : 256
npol : 1
nspectra : 120037408
poln_order : I
ra_deg : 149.05395833333333
snr : 6.763160000000001
snr_opt : -1
source_name : M82
tcand : 8230.16
time_decimation_factor : 1
tsamp : 0.000131072
tstart : 59485.58184027778
tstart_utc : 2021-09-28T13:57:51.000
width : 16

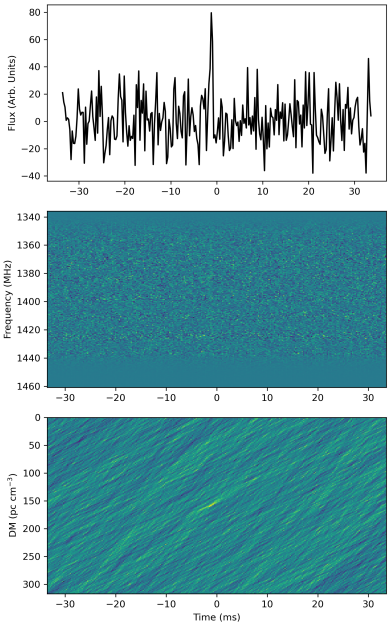

basename : Skynet_59488_M82_62247_11091_0001
bw : -125.0
cand_id : cand_tstart_59488.058402777780_tcand_9124.4200000_dm_158.65200_snr_6.36319
center_freq : 1398.388671875
dec_deg : 69.67958055555555
dm : 158.65200000000004
dm_opt : -1
dtype : uint16
fch1 : 1460.888671875
filename : Skynet_59488_M82_62247_11091_0001.fil
filepath : /notebook/scratch/M82/59488a
foff : -0.48828125
format : fil
frequency_decimation_factor : 1
gb : 40.61552588590964
gl : -38.63642466304424
label : 1
native_foff : -0.48828125
native_nchans : 256
native_nspectra : 274759808.0
native_tsamp : 0.000131072
nbits : 16
nchans : 256
npol : 1
nspectra : 274759808
poln_order : I
ra_deg : 149.14058333333335
snr : 6.36319
snr_opt : -1
source_name : M82
tcand : 9124.42
time_decimation_factor : 1
tsamp : 0.000131072
tstart : 59488.05840277778
tstart_utc : 2021-10-01T01:24:06.000
width : 4

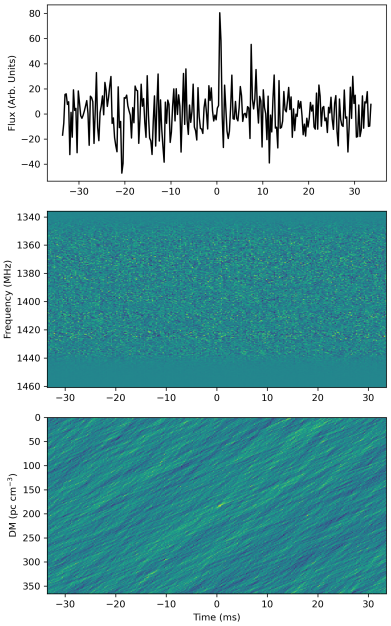

basename : Skynet_59488_M82_62270_11106_0001
bw : -125.0
cand_id : cand_tstart_59489.004155092596_tcand_7494.2800000_dm_183.09900_snr_6.45236
center_freq : 1398.388671875
dec_deg : 69.67978055555555
dm : 183.099
dm_opt : -1
dtype : uint16
fch1 : 1460.888671875
filename : Skynet_59488_M82_62270_11106_0001.fil
filepath : /notebook/scratch/M82/59488c
foff : -0.48828125
format : fil
frequency_decimation_factor : 1
gb : 40.583105266755155
gl : -38.60594053989607
label : 1
native_foff : -0.48828125
native_nchans : 256
native_nspectra : 274760512.0
native_tsamp : 0.000131072
nbits : 16
nchans : 256
npol : 1
nspectra : 274760512
poln_order : I
ra_deg : 149.02587500000004
snr : 6.45236
snr_opt : -1
source_name : M82
tcand : 7494.28
time_decimation_factor : 1
tsamp : 0.000131072
tstart : 59489.004155092596
tstart_utc : 2021-10-02T00:05:59.000
width : 4

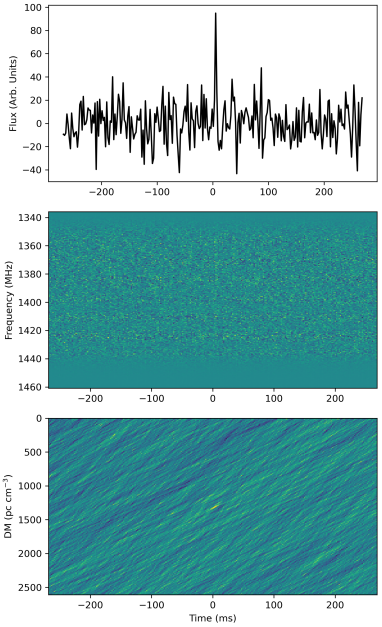

basename : Skynet_59496_M82_62300_11146_0001
bw : -125.0
cand_id : cand_tstart_59496.388483796298_tcand_2560.0000000_dm_1305.33000_snr_6.70110
center_freq : 1398.388671875
dec_deg : 69.67995833333333
dm : 1305.33
dm_opt : -1
dtype : uint16
fch1 : 1460.888671875
filename : Skynet_59496_M82_62300_11146_0001.fil
filepath : /notebook/scratch/M82/59496
foff : -0.48828125
format : fil
frequency_decimation_factor : 1
gb : 40.6170630732014
gl : -38.63850364491694
label : 1
native_foff : -0.48828125
native_nchans : 256
native_nspectra : 128568768.0
native_tsamp : 0.000131072
nbits : 16
nchans : 256
npol : 1
nspectra : 128568768
poln_order : I
ra_deg : 149.14683333333335
snr : 6.7011
snr_opt : -1
source_name : M82
tcand : 2560.0
time_decimation_factor : 1
tsamp : 0.000131072
tstart : 59496.3884837963
tstart_utc : 2021-10-09T09:19:25.000
width : 32

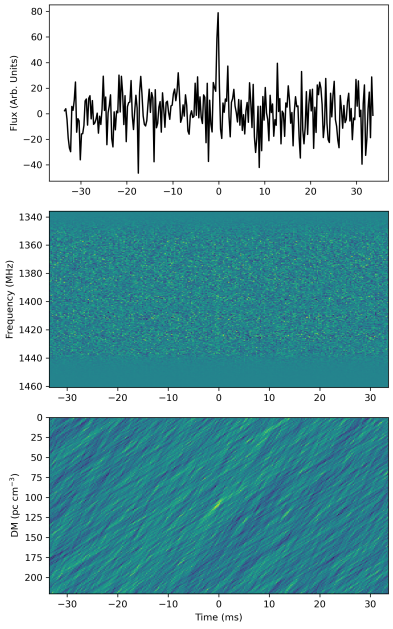

basename : Skynet_59506_M82_62423_11276_0001
bw : -125.0
cand_id : cand_tstart_59507.004861111112_tcand_1655.4800000_dm_110.19100_snr_6.45461
center_freq : 1398.388671875
dec_deg : 69.67970277777779
dm : 110.191
dm_opt : -1
dtype : uint16
fch1 : 1460.888671875
filename : Skynet_59506_M82_62423_11276_0001.fil
filepath : /notebook/scratch/M82/59506b
foff : -0.48828125
format : fil
frequency_decimation_factor : 1
gb : 40.58176494166368
gl : -38.60454409628895
label : 1
native_foff : -0.48828125
native_nchans : 256
native_nspectra : 274764864.0
native_tsamp : 0.000131072
nbits : 16
nchans : 256
npol : 1
nspectra : 274764864
poln_order : I
ra_deg : 149.02095833333334
snr : 6.45461
snr_opt : -1
source_name : M82
tcand : 1655.48
time_decimation_factor : 1
tsamp : 0.000131072
tstart : 59507.00486111111
tstart_utc : 2021-10-20T00:07:00.000
width : 4

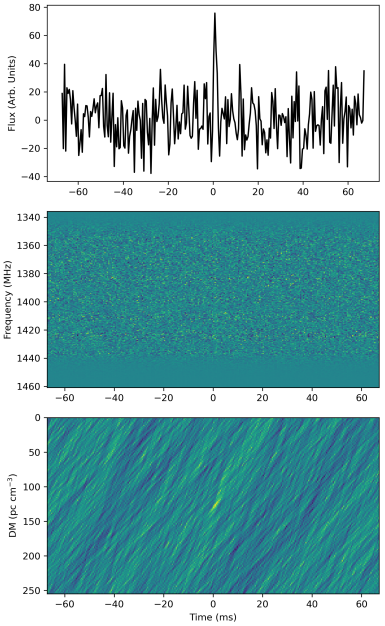

basename : Skynet_59506_M82_62423_11276_0001
bw : -125.0
cand_id : cand_tstart_59507.004861111112_tcand_22938.7000000_dm_127.46300_snr_6.11306
center_freq : 1398.388671875
dec_deg : 69.67970277777779
dm : 127.463
dm_opt : -1
dtype : uint16
fch1 : 1460.888671875
filename : Skynet_59506_M82_62423_11276_0001.fil
filepath : /notebook/scratch/M82/59506b
foff : -0.48828125
format : fil
frequency_decimation_factor : 1
gb : 40.58176494166368
gl : -38.60454409628895
label : 1
native_foff : -0.48828125
native_nchans : 256
native_nspectra : 274764864.0
native_tsamp : 0.000131072
nbits : 16
nchans : 256
npol : 1
nspectra : 274764864
poln_order : I
ra_deg : 149.02095833333334
snr : 6.11306
snr_opt : -1
source_name : M82
tcand : 22938.7
time_decimation_factor : 1
tsamp : 0.000131072
tstart : 59507.00486111111
tstart_utc : 2021-10-20T00:07:00.000
width : 8

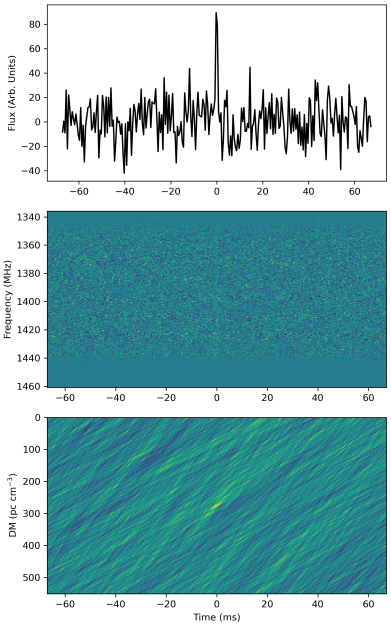

basename : Skynet_59514_M82_62541_11381_0001
bw : -125.0
cand_id : cand_tstart_59514.615902777776_tcand_6711.7400000_dm_275.54100_snr_7.49974
center_freq : 1398.388671875
dec_deg : 69.67963888888887
dm : 275.541
dm_opt : -1
dtype : uint16
fch1 : 1460.888671875
filename : Skynet_59514_M82_62541_11381_0001.fil
filepath : /notebook/scratch/M82/59514
foff : -0.48828125
format : fil
frequency_decimation_factor : 1
gb : 40.59130109307367
gl : -38.61348396154236
label : 1
native_foff : -0.48828125
native_nchans : 256
native_nspectra : 253188256.0
native_tsamp : 0.000131072
nbits : 16
nchans : 256
npol : 1
nspectra : 253188256
poln_order : I
ra_deg : 149.05466666666666
snr : 7.499739999999999
snr_opt : -1
source_name : M82
tcand : 6711.74
time_decimation_factor : 1
tsamp : 0.000131072
tstart : 59514.615902777776
tstart_utc : 2021-10-27T14:46:54.000
width : 8

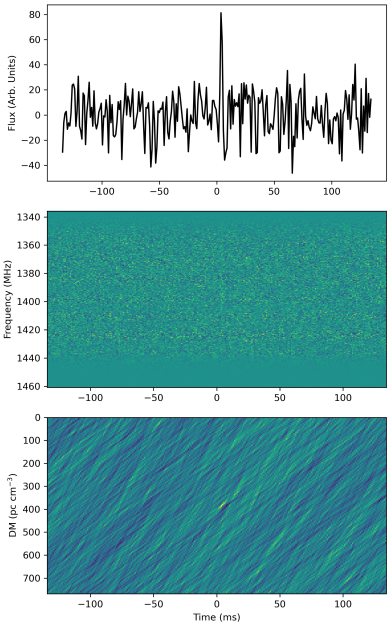

basename : Skynet_59515_M82_62541_11427_0001
bw : -125.0
cand_id : cand_tstart_59515.160879629628_tcand_3807.7900000_dm_384.30500_snr_6.60483
center_freq : 1398.388671875
dec_deg : 69.68013611111111
dm : 384.305
dm_opt : -1
dtype : uint16
fch1 : 1460.888671875
filename : Skynet_59515_M82_62541_11427_0001.fil
filepath : /notebook/scratch/M82/59515
foff : -0.48828125
format : fil
frequency_decimation_factor : 1
gb : 40.61559893486628
gl : -38.637397485800136
label : 1
native_foff : -0.48828125
native_nchans : 256
native_nspectra : 209238080.0
native_tsamp : 0.000131072
nbits : 16
nchans : 256
npol : 1
nspectra : 209238080
poln_order : I
ra_deg : 149.142
snr : 6.6048300000000015
snr_opt : -1
source_name : M82
tcand : 3807.79
time_decimation_factor : 1
tsamp : 0.000131072
tstart : 59515.16087962963
tstart_utc : 2021-10-28T03:51:40.000
width : 16

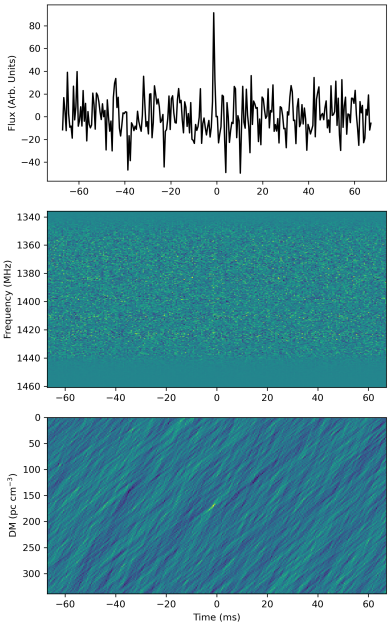

basename : Skynet_59516_M82_62541_11599_0001
bw : -125.0
cand_id : cand_tstart_59516.166307870371_tcand_7408.8900000_dm_169.43200_snr_6.71342
center_freq : 1398.388671875
dec_deg : 69.68006944444446
dm : 169.43200000000004
dm_opt : -1
dtype : uint16
fch1 : 1460.888671875
filename : Skynet_59516_M82_62541_11599_0001.fil
filepath : /notebook/scratch/M82/59516
foff : -0.48828125
format : fil
frequency_decimation_factor : 1
gb : 40.619987152984294
gl : -38.64147170964617
label : 1
native_foff : -0.48828125
native_nchans : 256
native_nspectra : 274760928.0
native_tsamp : 0.000131072
nbits : 16
nchans : 256
npol : 1
nspectra : 274760928
poln_order : I
ra_deg : 149.1574583333333
snr : 6.713419999999998
snr_opt : -1
source_name : M82
tcand : 7408.89
time_decimation_factor : 1
tsamp : 0.000131072
tstart : 59516.16630787037
tstart_utc : 2021-10-29T03:59:29.000
width : 8

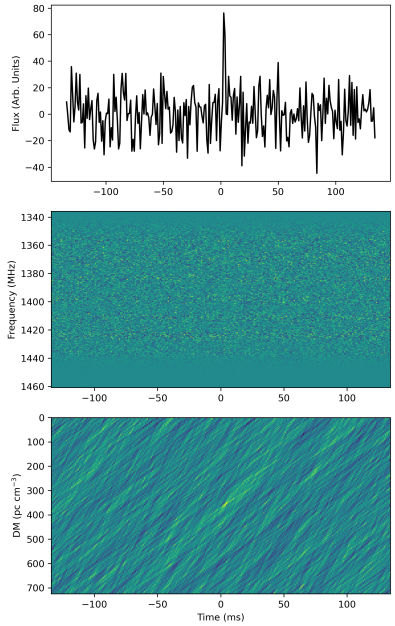

basename : Skynet_59521_M82_64504_12999_0001
bw : -125.0
cand_id : cand_tstart_59521.611064814817_tcand_1628.3900000_dm_362.35000_snr_6.16691
center_freq : 1398.388671875
dec_deg : 69.68025000000002
dm : 362.35
dm_opt : -1
dtype : uint16
fch1 : 1460.888671875
filename : Skynet_59521_M82_64504_12999_0001.fil
filepath : /notebook/scratch/M82/59521
foff : -0.48828125
format : fil
frequency_decimation_factor : 1
gb : 40.62008055641353
gl : -38.64185440562184
label : 1
native_foff : -0.48828125
native_nchans : 256
native_nspectra : 256386592.0
native_tsamp : 0.000131072
nbits : 16
nchans : 256
npol : 1
nspectra : 256386592
poln_order : I
ra_deg : 149.1581666666667
snr : 6.16691
snr_opt : -1
source_name : M82
tcand : 1628.39
time_decimation_factor : 1
tsamp : 0.000131072
tstart : 59521.61106481482
tstart_utc : 2021-11-03T14:39:56.000
width : 16

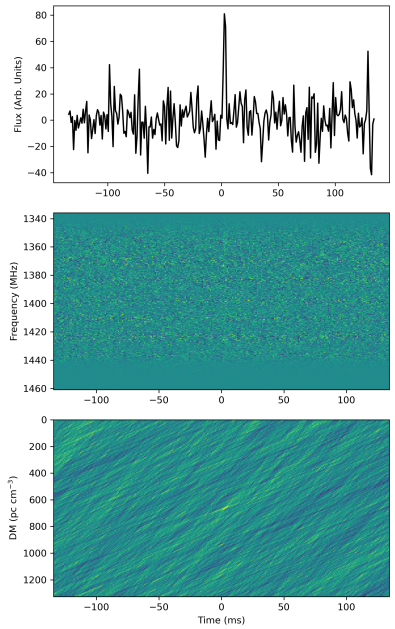

basename : Skynet_59536_M82_69557_18207_0001
bw : -125.0
cand_id : cand_tstart_59536.518657407411_tcand_7801.2700000_dm_663.36600_snr_6.62970
center_freq : 1398.388671875
dec_deg : 69.68002499999999
dm : 663.3660000000001
dm_opt : -1
dtype : uint16
fch1 : 1460.888671875
filename : Skynet_59536_M82_69557_18207_0001.fil
filepath : /notebook/scratch/M82/59536
foff : -0.48828125
format : fil
frequency_decimation_factor : 1
gb : 40.62140802367406
gl : -38.64275435144137
label : 1
native_foff : -0.48828125
native_nchans : 256
native_nspectra : 274765600.0
native_tsamp : 0.000131072
nbits : 16
nchans : 256
npol : 1
nspectra : 274765600
poln_order : I
ra_deg : 149.16241666666664
snr : 6.6297
snr_opt : -1
source_name : M82
tcand : 7801.27
time_decimation_factor : 1
tsamp : 0.000131072
tstart : 59536.51865740741
tstart_utc : 2021-11-18T12:26:52.000
width : 16

APPENDIX B: Bibliography

Agarwal, D., Aggarwal, K., Burke-Spolaor, S., Lorimer, D. R., & Garver-Daniels, N. 2020, MNRAS, 497, 1661, doi: 10.1093/mnras/staa1856

Barker, S., de Grijs, R., & Cerviño, M. 2008, A&A, 484, 711, doi: 10.1051/0004-6361:200809653

Barrau, A., Rovelli, C., & Vidotto, F. 2014, Phys. Rev. D, 90, 127503, doi: 10.1103/PhysRevD.90.127503

Barsdell, B. R., Bailes, M., Barnes, D. G., & Fluke, C. J. 2012, MNRAS, 422, 379, doi: 10.1111/j.1365-2966.2012.20622.x

Beloborodov, A. M. 2017, ApJ, 843, L26, doi: 10.3847/2041-8213/aa78f3

Bochenek, C. D., Ravi, V., Belov, K. V., et al. 2020, Nature, 587, 59, doi: 10.1038/s41586-020-2872-x

Boco, L., Lapi, A., Goswami, S., et al. 2019, ApJ, 881, 157, doi: 10.3847/1538-4357/ab328e

Brandenberger, R., Cyr, B., & Varna Iyer, A. 2017, arXiv e-prints, arXiv:1707.02397. https://arxiv.org/abs/1707.02397

Chatterjee, S., Law, C. J., Wharton, R. S., et al. 2017, Nature, 541, 58, doi: 10.1038/nature20797

CHIME/FRB Collaboration, Andersen, B. C., Bandura, K. M., et al. 2020, Nature, 587, 54, doi: 10.1038/s41586-020-2863-y

Comella, J. M., Craft, H. D., Lovelace, R. V. E., & Sutton, J. M. 1969, Nature, 221, 453, doi: 10.1038/221453a0

Cordes, J. M., & Lazio, T. J. W. 2002, arXiv e-prints, astro. https://arxiv.org/abs/astro-ph/0207156

Cordes, J. M., & Wasserman, I. 2016, MNRAS, 457, 232, doi: 10.1093/mnras/stv2948

Dai, Z. G., Wang, J. S., Wu, X. F., & Huang, Y. F. 2016, ApJ, 829, 27, doi: 10.3847/0004-637X/829/1/27

Falcke, H., & Rezzolla, L. 2014, A&A, 562, A137, doi: 10.1051/0004-6361/201321996

Fuller, J., & Ott, C. D. 2015, MNRAS, 450, L71, doi: 10.1093/mnrasl/slv049

Geng, J. J., & Huang, Y. F. 2015, ApJ, 809, 24, doi: 10.1088/0004-637X/809/1/24

Ghisellini, G. 2017, MNRAS, 465, L30, doi: 10.1093/mnrasl/slw202

Gu, W.-M., Dong, Y.-Z., Liu, T., Ma, R., & Wang, J. 2016, ApJ, 823, L28, doi: 10.3847/2041-8205/823/2/L28

Hawkins, T., & Lorimer, D. 2021, Department of Physics & Astronomy, Capstone Thesis, West Virginia University

Hewish, A., Bell, S. J., Pilkington, J. D. H., Scott, P. F., & Collins, R. A. 1968, Nature, 217, 709, doi: 10.1038/217709a0

Hurley-Walker, N., Zhang, X., Bahramian, A., et al. 2022, Nature, 601, 526, doi: 10.1038/s41586-021-04272-x

Kashiyama, K., & Murase, K. 2017, ApJ, 839, L3, doi: 10.3847/2041-8213/aa68e1

Kaspi, V. M., & Beloborodov, A. M. 2017, ARA&A, 55, 261, doi: 10.1146/annurev-astro-081915-023329

Katz, J. I. 2016, ApJ, 826, 226, doi: 10.3847/0004-637X/826/2/226

—. 2017, MNRAS, 469, L39, doi: 10.1093/mnrasl/slx052

Keane, E. F., Stappers, B. W., Kramer, M., & Lyne, A. G. 2012, MNRAS, 425, L71, doi: 10.1111/j.1745-3933.2012.01306.x

Kennicutt, Robert C., J., & De Los Reyes, M. A. C. 2021, ApJ, 908, 61, doi: 10.3847/1538-4357/abd3a2

Li, L.-B., Huang, Y.-F., Geng, J.-J., & Li, B. 2018, Research in Astronomy and Astrophysics, 18, 061, doi: 10.1088/1674-4527/18/6/61

Lingam, M., & Loeb, A. 2017, ApJ, 837, L23, doi: 10.3847/2041-8213/aa633e

Liu, X. 2018, Ap&SS, 363, 242, doi: 10.1007/s10509-018-3462-3

Lorimer, D. 2021, Nature Astronomy, 5, 870, doi: 10.1038/s41550-021-01465-2

Lorimer, D. R., Bailes, M., McLaughlin, M. A., Narkevic, D. J., & Crawford, F. 2007, Science, 318, 777, doi: 10.1126/science.1147532

Lorimer, D. R., & Kramer, M. 2004, Handbook of Pulsar Astronomy (Cambridge University Press)

Lyubarsky, Y. 2014, MNRAS, 442, L9, doi: 10.1093/mnrasl/slu046

Masui, K., & Chime/Frb Collaboration. 2021, in American Astronomical Society Meeting Abstracts, Vol. 53, American Astronomical Society Meeting Abstracts, 325.01

Metzger, B. D., Berger, E., & Margalit, B. 2017, ApJ, 841, 14, doi: 10.3847/1538-4357/aa633d

Metzger, B. D., Margalit, B., & Sironi, L. 2019, MNRAS, 485, 4091, doi: 10.1093/mnras/stz700

Mingarelli, C. M. F., Levin, J., & Lazio, T. J. W. 2015, ApJ, 814, L20, doi: 10.1088/2041-8205/814/2/L20

Murase, K., Kashiyama, K., & Mészáros, P. 2016, MNRAS, 461, 1498, doi: 10.1093/mnras/stw1328

Petroff, E., Hessels, J., & Lorimer, D. 2019, The Astronomy and Astrophysics Review, 27, 75, doi: 10.1007/s00159-019-0116-6

Petroff, E., Hessels, J. W. T., & Lorimer, D. R. 2021, arXiv eprint

Popov, S. B., & Postnov, K. A. 2010, in Evolution of Cosmic Objects through their Physical Activity, ed. H. A. Harutyunian, A. M. Mickaelian, & Y. Terzian, 129–132. https://arxiv.org/abs/0710.2006

Punsly, B., & Bini, D. 2016, MNRAS, 459, L41, doi: 10.1093/mnrasl/slw039

Raby, S. 2016, Phys. Rev. D, 94, 103004, doi: 10.1103/PhysRevD.94.103004

Spanakis-Misirlis, A. 2021, FRBSTATS: A web-based platform for visualization of fast radio burst properties. http://ascl.net/2106.028

Spitler, L. G., Scholz, P., Hessels, J. W. T., et al. 2016, Nature, 531, 202, doi: 10.1038/nature17168

Staelin, D. H., & Reifenstein, Edward C., I. 1968, Science, 162, 1481, doi: 10.1126/science.162.3861.1481

Tendulkar, S. P., Bassa, C. G., Cordes, J. M., et al. 2017, ApJ, 834, L7, doi: 10.3847/2041-8213/834/2/L7

Totani, T. 2013, PASJ, 65, L12, doi: 10.1093/pasj/65.5.L12

Zhong, S.-Q., Xie, W.-J., Deng, C.-M., et al. 2022, arXiv e-prints, arXiv:2202.04422. https://arxiv.org/abs/2202.04422